Supplementary Material

COSTA MODEL

A hierarchical carbonate reservoir benchmarking case study for reservoir characterisation, uncertainty quantification & history matching.

Jorge Costa Gomes, Sebastian Geiger & Daniel Arnold

Institute of GeoEnergy Engineering, Heriot-Watt University, UK

COSTA MODEL
C – Costa
O – Offers
S – Subsurface
T – Type
A – Analogue Model

Which is
C – Comprehensive
O – Objective
S – Specific
T – Tested
A – Applied

Integrating
C – Cores
O – Open-hole Logs
S – Sequence Stratigraphy
T – Test Data
A – Attributes

Further published material:

J. Costa Gomes, S. Geiger, and D. P. Arnold, "A Hierarchical Carbonate Reservoir Benchmarking Case Study for Reservoir Characterisation, Uncertainty Quantification & History Matching," in *81st EAGE Conference and Exhibition*, London, 2019: EAGE, doi: 10.3997/2214-4609.201901631

J. Costa Gomes, S. Geiger, and D. P. Arnold, "An Open Access Carbonate Reservoir Benchmarking Study for Reservoir Characterisation, Uncertainty Quantification & History Matching," presented at the SPE Reservoir Characterisation and Simulation Conference and Exhibition, Abu Dhabi, UAE, 2019. SPE-196674-MS

J. Costa Gomes, Geiger, S. Geiger, and D. P. Arnold. "Using Synthetic Production Data from an Open Source Carbonate Reservoir Model to Improve our Understanding of Flow Behaviour." Paper presented at the SPE Europec featured at 82nd EAGE Conference and Exhibition, Amsterdam, The Netherlands, December 2020. doi: https://doi.org/10.2118/200586-MS

DOI: 10.17861/6e36e28d-50d9-4e31-9790-18db4bce6e5d

Supplementary Material

Table of Contents

List of Tables **3**
List of Figures **3**
1. Introduction **6**
2. Model Construction **7**
2.1 Framework Modelling 7
2.2 Flow Unit Architectures 7
2.3 Synthetic SCAL Database 9
2.4 Petrophysical Modelling 12
2.5 Synthetic Well Logs 14
2.6 Saturation Height Modelling 15
2.7 Reservoir Characteristics 18
2.8 Dynamic Reservoir Properties 24
3. Reservoir Model Description **28**
3.1 Subsectors 30
3.2 Skin Effect 31
3.3 RRT Effect 32
3.4 Grid Refinement & Ultimate Recovery Factor 36
3.5 Synthetic Production Data 37
4. Understanding the Data **38**
5. References **40**

DOI: 10.17861/6e36e28d-50d9-4e31-9790-18db4bce6e5d

Supplementary Material

List of Tables

Table 1: Geological characteristics of the wells used to construct the closure of interest. 7
Table 2: Modelling approach 13
Table 3: Rearrangement of Archie's equation. 14
Table 4: Correlations between relative permeability and wettability index. 25
Table 5: Dynamic characteristics of our 27 reservoir rock types for reservoir simulation. Conditional colours were applied to the wettability index column. USBM wettability index values range from strongly water wet (dark blue) to strongly oil wet (dark red). 27
Table 6: Dynamic reservoir model description for one ensemble member. 28
Table 7: Well controls for the initial full field development plan. A conservative BHP regulated production constraint was set to all the producers to be 334 psi above the bubble point. All water injectors were constrained only by BHP of 6,000 psi to be under the synthetic fracking pressure of this reservoir. 29

List of Figures

Figure 1: Extracted sector model for reservoir simulation and synthetic production data acquisition. [Left] Showcased is the areal map of oil saturation for the full COSTA model; [centre] top depth map of the field development plan of the sector and; [right] the field pressure in year 2040. 6
Figure 2: Uncertainty inherent to modelling the topography of the surfaces. Example of a surface based on well tops alone [left] and a surface based on both well tops and synthetic contour map [right]. 7
Figure 3: Lorenz plots for all wells used to construct the full-sized model [left] and Lorenz plots for the closure depicted in Figure 1 and 4 from which the synthetic production data was generated [right]. 8
Figure 4: Shelf-to-basin cumulative flow and storage capacity capturing multiple vertical and lateral heterogeneities along with variable baffle zone thicknesses. Three geological closures are shown to demonstrate the general heterogeneity of oil saturation distribution found across the model. Highlighted in red is the area we targeted first to generate the synthetic production data. 8
Figure 5: Synthetic SCAL database which consists of 110 carbonate plug sample MICP mimicked data. Showcased in column 1 are the capillary pressure data at two different maximum pressures of 40 and 120 psi (equivalent to 310 and 930 ft height above FWL respectively) and column 2 showcases the MICP PTSDs original versus normalized data. 9
Figure 6: 27 RRTs with a selection of at least 3 drainage capillary pressure curves for each. A 'truth' combination for model initialization has been selected. There are over 53 trillion model initialization scenarios. Y-axis is limited to a maximum of 40 psi which is equivalent to a height above FWL of 310 ft Winland R35 ranges increasing from RRT 1 (0 – 0.2 µm) to RRT 27 (>7 µm). 10
Figure 7: Cross plots for the 110 mercury injection capillary pressure data included in the open-source dataset [left column]. 27 Winland R35 poro-perm transforms range from 0.1 to 7 µm. Three selected reservoir rock types with a minimum of three samples per reservoir rock type [right column]. Note the wide range of capillary threshold pressures (from 1 to 20 psi), as well as porosity and permeabilities and pore throat size distributions (from unimodal to trimodal). 11
Figure 8: Raw porosity vs. permeability cross plot before well upscaling [top], 27 Winland R35 PTSD ranges (0 to 7 µm) [centre] and conformed bivariate distribution of porosity and

DOI: 10.17861/6e36e28d-50d9-4e31-9790-18db4bce6e5d

permeability according to the 27 Winland R35 pore throat size ranges and trending spatially by honouring the facies map [bottom]. 12
Figure 9: Continuous distribution of mean pore throat size distribution (microns) across the entire model [A]. Discrete distribution of 27 grouped micron ranges from 0 to 7 µm [B]. 13
Figure 10: Synthetic water saturation profiles created for wells without resistivity data using a GRG Nonlinear Solver to back calculate the appropriate trends of petrophysical data for a given water saturation profile. 14
Figure 11: Eight example well logs and 3 tracks at multiple heights above the FWL. Height above the FWL (0 to 545 ft) [1st track], distribution of 27 reservoir rock types (1 to 27) [2nd track] and water saturation derived from our saturation height functions (upscaled) and the open-hole logs (continuous black line) [3rd track]. Water saturation ranges from 100% (blue) to 0% (dark orange). The reservoir rock typing methodology and the saturation height functions used have a good match with the water saturation derived from the open-hole logs. Scale fixed at 1:220 ft true vertical depth sub-sea. Depth is hidden in order to conceal the FWL of our truth case. 16
Figure 12: Eight example well logs and 11 tracks from multiple heights above the FWL. Height above the FWL (0 to 545 ft) [1st], gamma ray (2.2 to 27 gAPI) [2nd], density (2.1 to 2.7 g/cm^3) [3rd], density (1.9 to 2.9 g/cm^3) vs. neutron porosity (-0.15 to 0.45 ft^3/ft^3) [4th], neutron porosity (0.05 to 0.4 ft^3/ft^3) [5th], cored porosity (5 to 40 ft^3/ft^3) [6th], cored porosity vs. neutron porosity [7th], cored permeability (0.1 to 500 mD) [8th], formation resistivity (0.2 to 200 ohm) [9th], water saturation (0 to 100%) from saturation height functions (upscaled) and open-hole log water saturation (continuous black line) [10th] and reservoir rock types (1 to 27) [11th]. Scale fixed at 1:280 ft true vertical depth sub-sea (depth hidden). 17
Figure 13: Wells and coordinates [left] and top depth map with synthetic contour lines [right]. The red line shows the 180 km cross section depicted in Figure 14 and Figure 15. 18
Figure 14: Cross sections (southwest to northeast ~180 km) showcasing multiple vertical and lateral petrophysical properties across the three structural closures found in our truth case. Density (2.1 to 2.7 g/cm^3) [A], gamma ray (2.2 to 70 gAPI) [B], porosity (0.05 to 0.35 ft^3/ft^3) [C], permeability (0.1 to 1500 mD) [D] and cementation exponent *m* (1 to 4.5) [E]. Our undisclosed free water level is exemplified as the black horizontal line (formation depth is hidden). 19
Figure 15: Cross sections (southwest to northeast ~180 km) showcasing multiple vertical and lateral petrophysical properties across the three structural closures found in our truth case. Saturation exponent *n* (1 to 4.5) [F], reservoir quality index (0 to 4.5) [G], Winland R35 mean pore throat size (0.1 to 7 µm) [H], reservoir rock types (1 to 27) [I] and water saturation (0 to 100%) [J]. Our undisclosed free water level is exemplified as the black horizontal line (formation depth is hidden). 20
Figure 16: Lithology example of one particular well. 21
Figure 17: Well coordinates for all 43 wells used in this study along with the general location of the regional depositional environments. Highlighted in red are the six selected wells depicted in Figure 18 which highlight the regional heterogeneity variation across our model. The flow unit architectures across all wells are diverse but generally there is a trend; a more uniform flow and storage capacity in the shelf and basin areas and a more heterogeneous contrast in and around the platform interior – margin areas. 21
Figure 18: Regional flow unit architectures across the shelf-to-basin profile (Figure 17). Stratigraphic flow profiles have a normalized cumulative flow capacity (blue) and storage capacity (red) with respect to true vertical depth sub-sea. 22
Figure 19: Key reservoir characteristics of all 43 wells used in this study ordered from lowest y-northing to highest y-northing (from shelf to basin). The six wells shown in Figure 17 and Figure 18 are also highlighted in red (x-axis). 23

DOI: 10.17861/6e36e28d-50d9-4e31-9790-18db4bce6e5d

Supplementary Material

Figure 20: Drainage capillary pressure curves honouring irreducible water saturation cut-offs [top], the relative permeability of oil (green) and water (red) [centre], and forced imbibition capillary pressure curves honouring irreducible water saturation and residual oil saturation after waterflood cut-offs [bottom]. 24
Figure 21: United States Bureau of Mines wettability index per reservoir rock type honouring the wettability, irreducible water saturation, and residual oil saturation after waterflood in the relative permeability curves. 25
Figure 22: Synthetic relationship used between irreducible water saturation and residual oil saturation after waterflood for each reservoir rock type. 26
Figure 23: Location of our seven subsectors (C1 – C7) [left] and their field performances [right]. The subsectors incorporate the same field development plan with all 144 ensemble members and therefore some subsectors e.g., C3 start producing at a much later date (2040). 30
Figure 77: Field performance comparison of a case with zero skin (solid lines) and case with positive and negative skin randomly selected for each of the individual 248 producing wells (dashed lines) [left]. An example of a single producer well with a negative skin (solid line) helping improve the oil production rate [right]..... 31
Figure 78: Field performance and reservoir characterisation of a single ensemble member with four clustered reservoir rock type maps; 27 RRTs [red], 7 RRTs [blue], 5 RRTs [orange] and 3 RRTs [green]. Oil production rate [A], oil production cumulative [B], oil recovery factor [C], water-cut [D], average field oil saturation with height above the FWL [E], rock type distribution along a single well [F], average field relative permeability to water at irreducible oil [G] and average field maximum oil-water capillary pressure [H]..... 32
Figure 53: Laterally averaged properties for a given reservoir layer across all ensemble members with 7 RRTs. Differences in net pore volume, gross block volume and grid thickness are associated with having two different stratigraphic frameworks concepts e.g., the interpretation of the formation tops, baffle tops and their respective thicknesses. Wide range of average field values for porosity are due to the use of wireline or cored values. Permeability profiles vary due to the well-log upscaling technique used and spatial modelling approach (linked to facies maps). Both porosity and permeability have also been modelled with a reduced horizontal anisotropic range. Differences in oil per unit area (layer), oil per unit area (total), average field maximum oil-water capillary pressure, and average field relative permeability to water at irreducible oil are also demonstrated. 33
Figure 54: Laterally averaged properties for a given reservoir layer for all ensemble members with a variable number of reservoir rock types e.g., 3, 5, 7 and 27 RRTs showing the differences in oil per unit area (layer), oil per unit area (total), maximum water-oil capillary pressure and relative permeability of water at irreducible oil with respect to reservoir height. 34
Figure 55: Distribution of relative permeability of water at irreducible oil and reservoir rock types along well HW-10. The seven relative permeability curves used in this particular ensemble member are also shown. Wettability varies from strongly water-wet (RRT 1) to strongly oil-wet (RRT 7)..... 35
Figure 79: Field performance affected by grid refinement for one ensemble member. Original model grid dimension 250 x 250 m [blue], 125 x 125 m [red] and 62.5 x 62.5 m [green]. 36
Figure 81: Ultimate recovery factor and field performance affected by grid refinement for one ensemble member. Original model grid dimension 250 x 250 m [blue], 125 x 125 m [red] and 62.5 x 62.5 m [green]. 36
Figure 89: Random Gaussian noise added synthetic production data. Showcased side-by-side are zoomed in time sections for a particular well. 37

DOI: 10.17861/6e36e28d-50d9-4e31-9790-18db4bce6e5d

Supplementary Material

COSTA MODEL

A hierarchical carbonate reservoir benchmarking case study for reservoir characterisation, uncertainty quantification & history matching.

Jorge Costa Gomes, Sebastian Geiger & Daniel Arnold

Institute of GeoEnergy Engineering, Heriot-Watt University, UK

1. Introduction

The COSTA model is an open-source carbonate reservoir case study that uniquely considers major uncertainties inherent to carbonate reservoirs using one of the most prolific aggradational parasequence carbonate formation sets in the Rub Al Khali basin, the Upper Kharaib Member (Early Cretaceous), as an analogue. The novelty of our work is the provision of a unique open access dataset which enables reproducible science in the field of reservoir characterisation and simulation, and helps train new generations of geoscientists and reservoir engineers in the art of characterising, simulating and predicting the reservoir performance of carbonate reservoirs under different recovery processes.

Our models use fully anonymized, rescaled, repositioned and structurally deformed subsurface data from 43 wells across multiple fields in the Rub Al Khali basin from different geo-depositional settings, encompassing various facies, and a variety of petrophysical properties and hydrocarbon columns above the free water level (FWL). The resulting models, which have a unique coordinate system, comprise of three main anticlines which form individual reservoirs that can be extracted for reservoir simulation and engineering studies. Synthetic production data has been generated from one of the anticlines by adding wells to an undisclosed 'truth case' model to obtain field-wide and well-by-well production data (oil, gas, and water rates, bottom-hole pressures etc.) for history matching purposes.

The aim of this work has been to create an open access reservoir modelling case study that considers the major ranges of interpretational uncertainties inherent to carbonate reservoirs and provide our industry with 144 pre-built reservoir models which considers both, interpretational scenarios and multiple choices of geomodelling techniques. Moreover, the integrated models attempt to capture the main reservoir architectures (stratal geometries), facies, pore systems, diagenetic overprints and wettability variations across the most prolific carbonate oil reservoirs in the Rub Al Khali basin – the Upper Kharaib Member (Early Cretaceous) as an analogue.

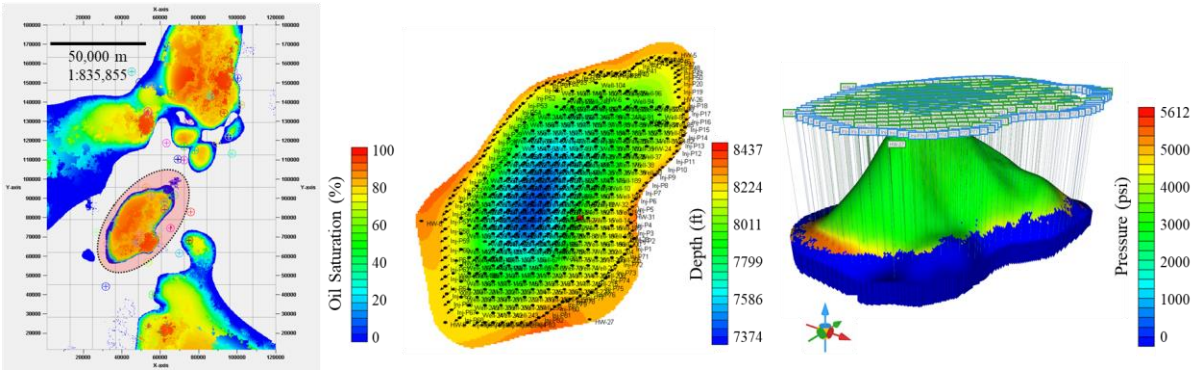

Figure 1: Extracted sector model for reservoir simulation and synthetic production data acquisition. [Left] Showcased is the areal map of oil saturation for the full COSTA model; [centre] top depth map of the field development plan of the sector and; [right] the field pressure in year 2040.

DOI: 10.17861/6e36e28d-50d9-4e31-9790-18db4bce6e5d

Supplementary Material

2. Model Construction

2.1 Framework Modelling

Modelling the surfaces i.e., surfaces based on well tops versus surfaces based on both well tops and digitized contour maps. Each provide a unique structural interpretation map not to mention the chosen modelling algorithm (i.e., convergent, least squares etc). In this study we provide two unique contour map interpretations for those willing to rebuild their own geological models.

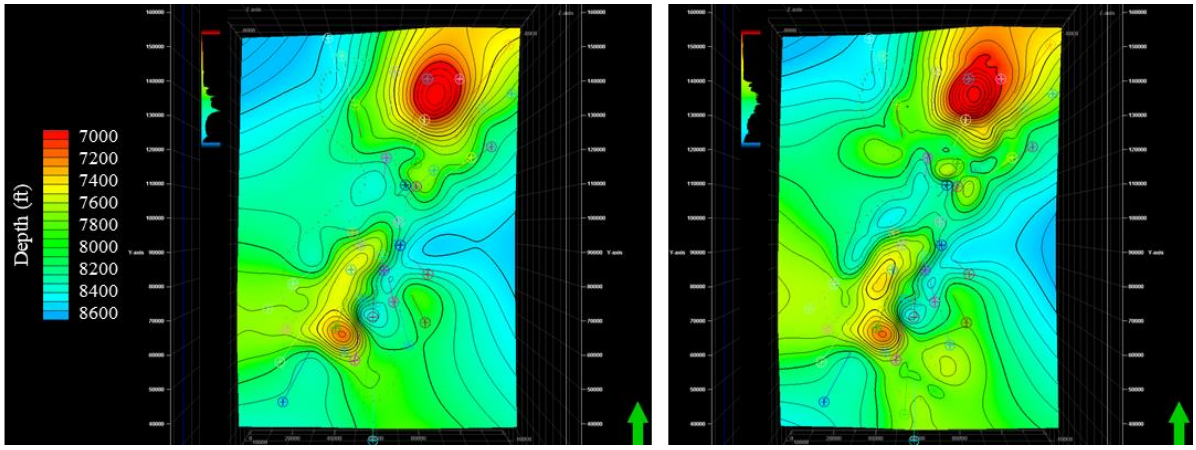

Figure 2: Uncertainty inherent to modelling the topography of the surfaces. Example of a surface based on well tops alone [left] and a surface based on both well tops and synthetic contour map [right].

2.2 Flow Unit Architectures

Table 1: Geological characteristics of the wells used to construct the closure of interest.

Well No.	Original Structural Position	Lorenz Coefficient	Cv (Porosity)	Cv (Permeability)	Avg. Porosity (%)	Avg. Permeability (mD)	Reservoir Thickness (ft)
HW-3	Oil Zone	0.59	0.40	1.63	23.8	27.05	117
HW-4	Downflank (TZ)	0.71	0.46	3.06	13.2	28.66	155
HW-5	Downflank (TZ)	0.42	0.55	1.79	7.0	0.39	138
HW-6	Oil Zone	0.56	0.42	1.51	18.1	17.94	157
HW-7	Downflank (TZ)	0.69	0.35	2.11	15.2	10.08	146
HW-8	Below FWL	0.69	0.31	2.96	16.7	17.07	120
HW-9	Downflank (TZ)	0.63	0.32	1.95	17.1	14.45	143
HW-10	Mid Flank	0.57	0.31	1.33	18.4	10.54	157
HW-24	Oil Zone	0.53	0.40	1.41	18.2	7.14	162
HW-25	Oil Zone	0.26	0.43	0.88	18.4	3.09	152
HW-26	Mid Flank	0.48	0.44	1.52	10.8	1.41	175
HW-27	Below FWL	0.69	0.38	2.05	18.7	7.88	176
HW-28	Mid Flank	0.63	0.35	1.62	17.1	19.42	196
HW-29	Oil Zone	0.62	0.35	1.62	26.1	39.20	214
HW-30	Oil Zone	0.68	0.17	2.26	26.8	48.01	177
HW-31	Below FWL	0.64	0.25	1.85	18.9	23.46	181
HW-32	Oil Zone	0.59	0.31	1.56	24.7	43.87	161

DOI: 10.17861/6e36e28d-50d9-4e31-9790-18db4bce6e5d

Supplementary Material

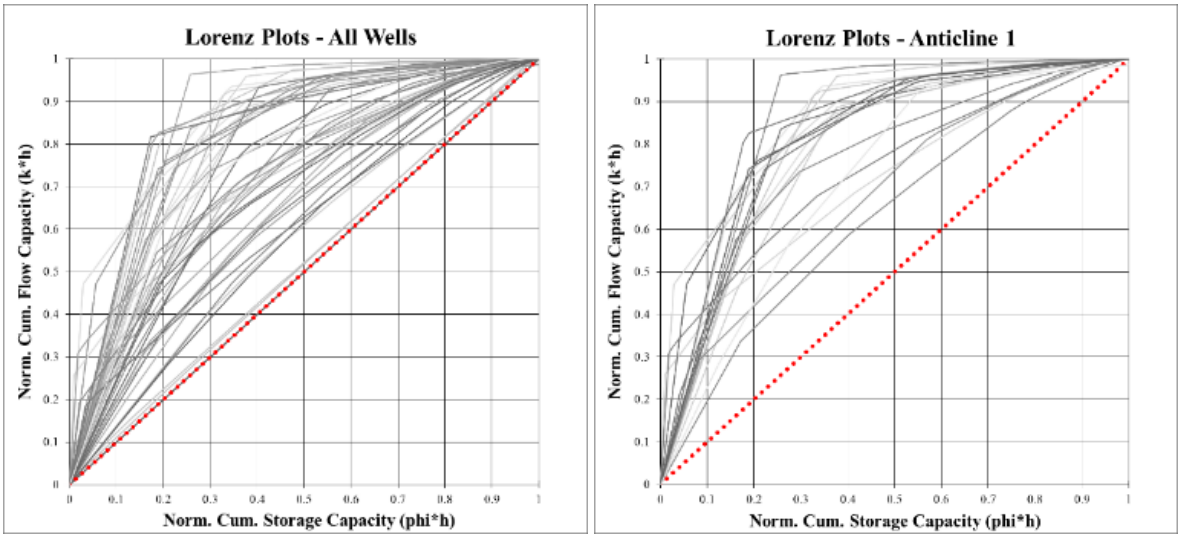

Figure 3: Lorenz plots for all wells used to construct the full-sized model [left] and Lorenz plots for the closure depicted in Figure 1 and 4 from which the synthetic production data was generated [right].

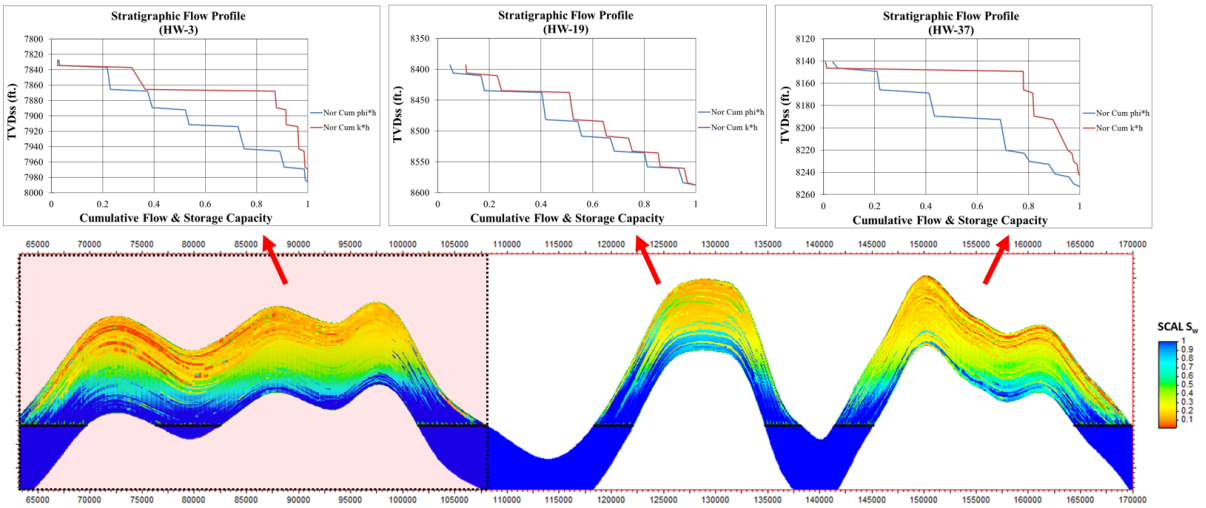

Figure 4: Shelf-to-basin cumulative flow and storage capacity capturing multiple vertical and lateral heterogeneities along with variable baffle zone thicknesses. Three geological closures are shown to demonstrate the general heterogeneity of oil saturation distribution found across the model. Highlighted in red is the area we targeted first to generate the synthetic production data.

DOI: 10.17861/6e36e28d-50d9-4e31-9790-18db4bce6e5d

Supplementary Material

2.3 Synthetic SCAL Database

Our synthetic SCAL database, which is part of the released data, contains 110 capillary pressure and PTSD curves from anonymized MICP data measured for a wide range of carbonate plug samples, all linked to porosity, permeability and Winland R35 values. Unimodal, bimodal, and trimodal PTSDs are present in the dataset, capturing multiple realistic drainage capillary pressure curves for a wide range of carbonate pore fabrics. The open-source provision of the underpinning raw data enables users to analyse the impact of using different saturation height modelling functions on STOIIP and production.

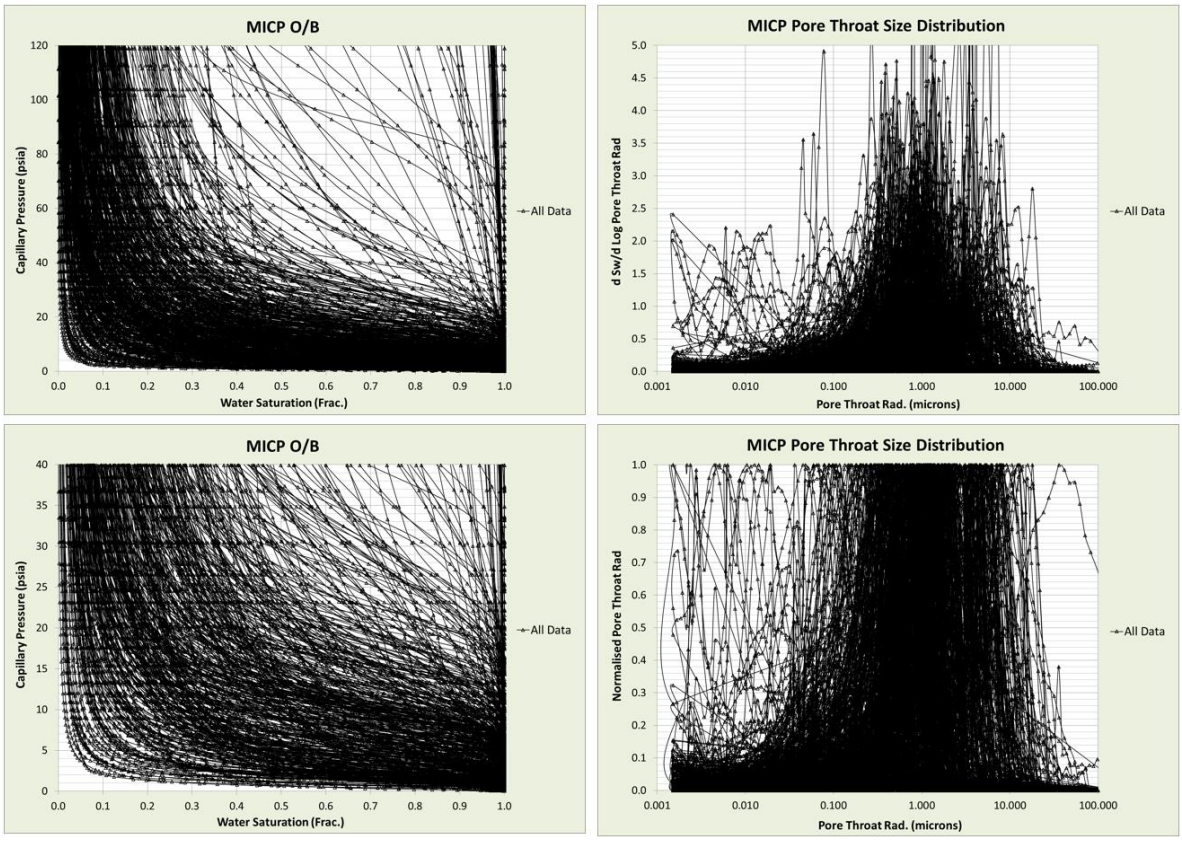

Figure 5: Synthetic SCAL database which consists of 110 carbonate plug sample MICP mimicked data. Showcased in column 1 are the capillary pressure data at two different maximum pressures of 40 and 120 psi (equivalent to 310 and 930 ft height above FWL respectively) and column 2 showcases the MICP PTSDs original versus normalized data.

DOI: 10.17861/6e36e28d-50d9-4e31-9790-18db4bce6e5d

Supplementary Material

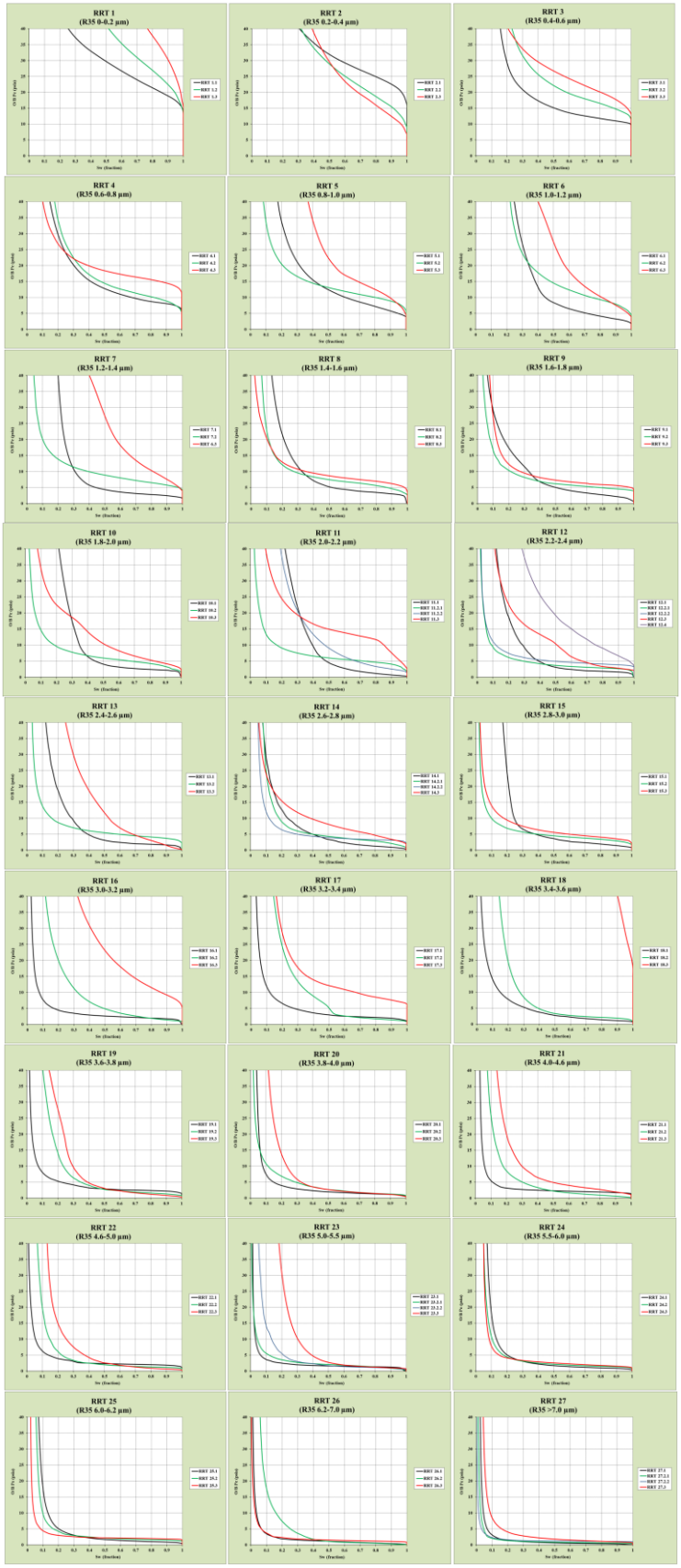

Figure 6: 27 RRTs with a selection of at least 3 drainage capillary pressure curves for each. A 'truth' combination for model initialization has been selected. There are over 53 trillion model initialization scenarios. Y-axis is limited to a maximum of 40 psi which is equivalent to a height above FWL of 310 ft Winland R35 ranges increasing from RRT 1 (0 – 0.2 µm) to RRT 27 (>7 µm).

DOI: 10.17861/6e36e28d-50d9-4e31-9790-18db4bce6e5d

Supplementary Material

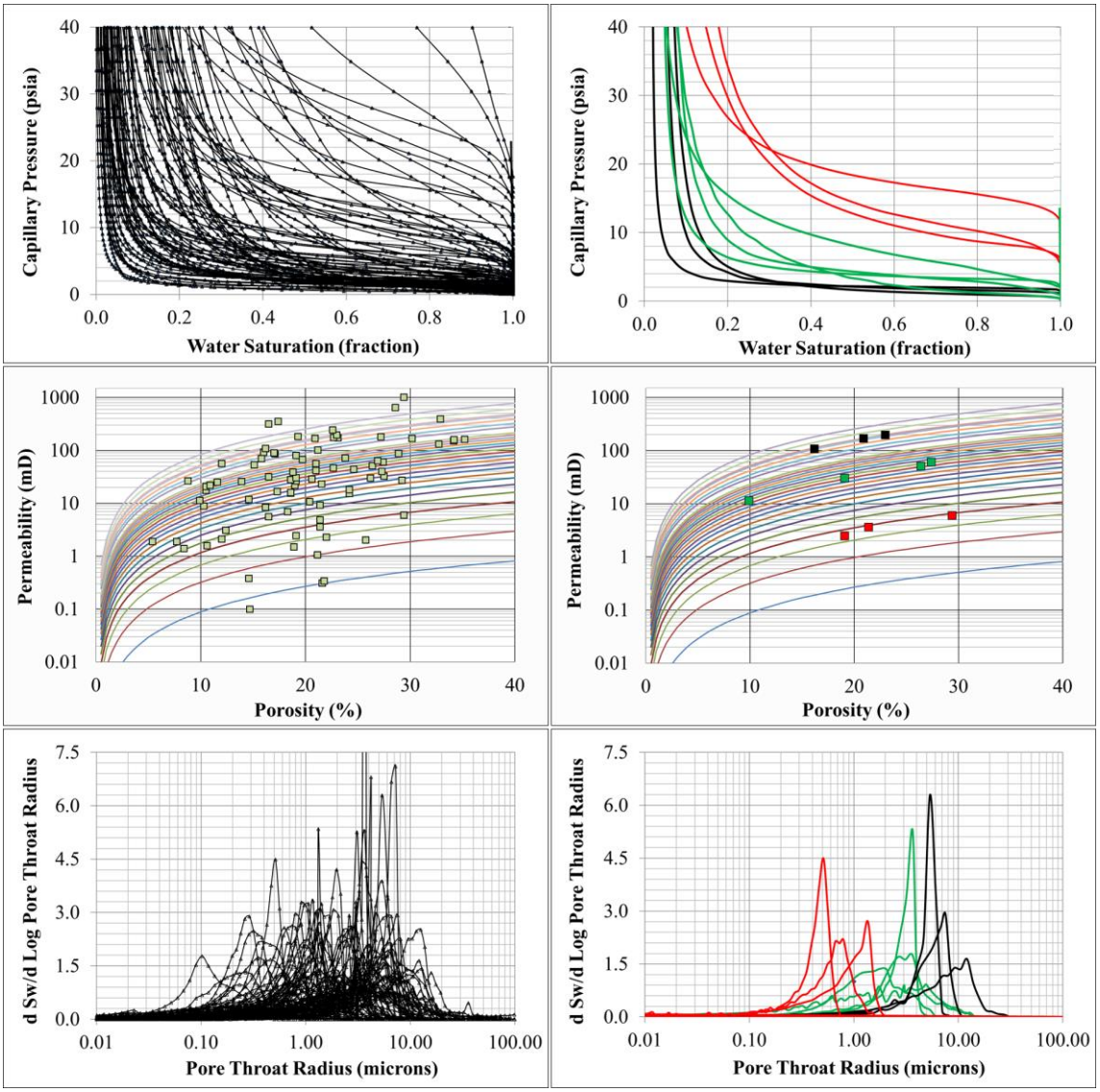

Figure 7: Cross plots for the 110 mercury injection capillary pressure data included in the open-source dataset [left column]. 27 Winland R35 poro-perm transforms range from 0.1 to 7 μm. Three selected reservoir rock types with a minimum of three samples per reservoir rock type [right column]. Note the wide range of capillary threshold pressures (from 1 to 20 psi), as well as porosity and permeabilities and pore throat size distributions (from unimodal to trimodal).

DOI: 10.17861/6e36e28d-50d9-4e31-9790-18db4bce6e5d

Supplementary Material

2.4 Petrophysical Modelling

A 3D collocated co-kriging (or bivariate distribution) Sequential Gaussian Simulation (SGS) distribution relating porosity and permeability was established such that both independent values are honouring the geological trends of the RRT maps. To achieve this, cross-plots of multiple pore throat size distribution ranges from Winland R35 were created and used as a constraint for the spatial trends in the petrophysical data.

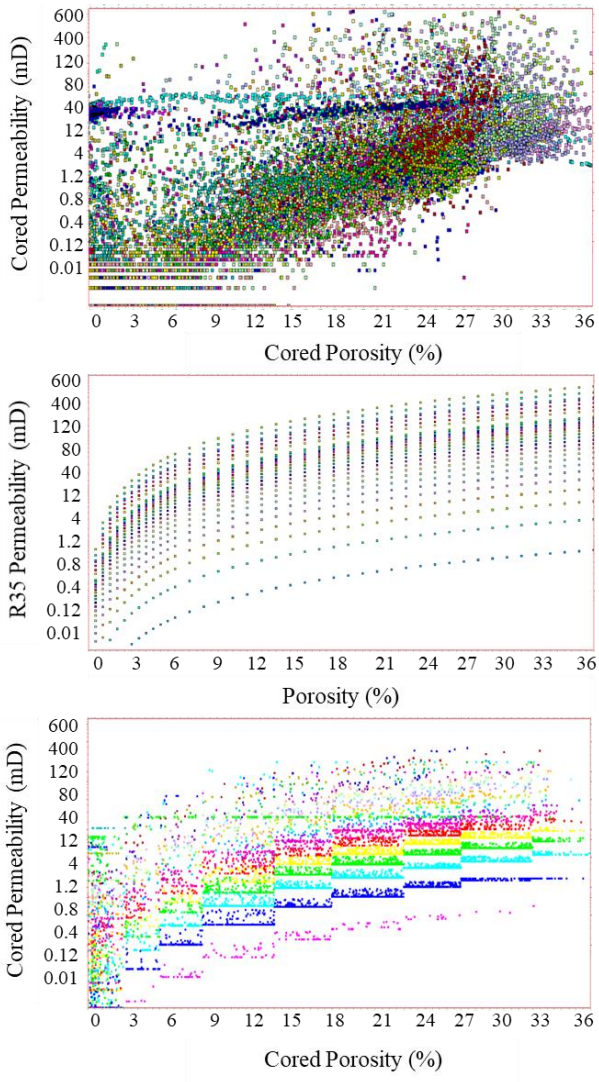

Figure 8: Raw porosity vs. permeability cross plot before well upscaling [top], 27 Winland R35 PTSD ranges (0 to 7 µm) [centre] and conformed bivariate distribution of porosity and permeability according to the 27 Winland R35 pore throat size ranges and trending spatially by honouring the facies map [bottom].

Once an arbitary relationship between porosity and permeability was established using 27 Winland R35 ranges (0 – 7 µm) the next stage was to convert continuous data into discrete data (RRTs). For this purpose the Winland R35 values were first calculated as follows [2];

$$Winland\ R35 = 10^{(0.538*\log k - 0.864*\log \phi)+0.731} \quad (1)$$

The 27 discrete RRTs were then assigned according to the arbitrary ranges of mean PTSDs shown in Table 4.

DOI: 10.17861/6e36e28d-50d9-4e31-9790-18db4bce6e5d

Supplementary Material

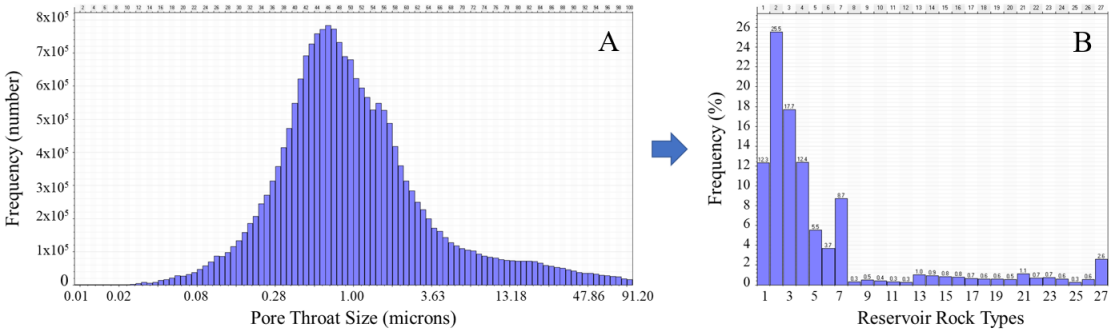

Figure 9: Continuous distribution of mean pore throat size distribution (microns) across the entire model [A]. Discrete distribution of 27 grouped micron ranges from 0 to 7 µm [B].

Table 2: Modelling approach

Property	Modelling Approach
Porosity	SGS
Permeability	SGS & Collocated Co-Kriging SGS
Facies / RRTs	Winland R35 PTSD
Water Saturation	Skelt-Harrison

DOI: 10.17861/6e36e28d-50d9-4e31-9790-18db4bce6e5d

Supplementary Material

2.5 Synthetic Well Logs

Synthetic water saturation (S_w) for wells without resistivity measurements (R_t) has been computed using a Generalized Reduced Gradient (GRG) Nonlinear Solver, which attempted to back calculate the most appropriate R_t value for a given S_w profile. The solution of computing a synthetic S_w profile by rearranging Archie's saturation variables was non-unique. Archie's equation is given by [1]

$$S_w = \left(\frac{1}{\phi^m} * \frac{R_w}{R_t}\right)^{\frac{1}{n}}, \tag{2}$$

where m is the cementation exponent (function of tortuosity), n is the saturation exponent (function of wettability), R_w is the resistivity of formation brine, R_t is the true resistivity of formation (virgin zone) and ϕ is porosity.

Table 3: Rearrangement of Archie's equation.

$R_t = \left(\frac{1}{\phi^m} * \frac{R_w}{{S_w}^n}\right)$	$R_w = \phi^m * R_t * {S_w}^n$	$n = \frac{\log\left(\frac{1}{\phi^m} * \frac{R_w}{R_t}\right)}{\log S_w}$	$m = \frac{\log\left(\frac{1}{{S_w}^n} * \frac{R_w}{R_t}\right)}{\log \phi}$	$\phi = \left(\frac{R_w}{R_t * {S_w}^n}\right)^{\frac{1}{m}}$

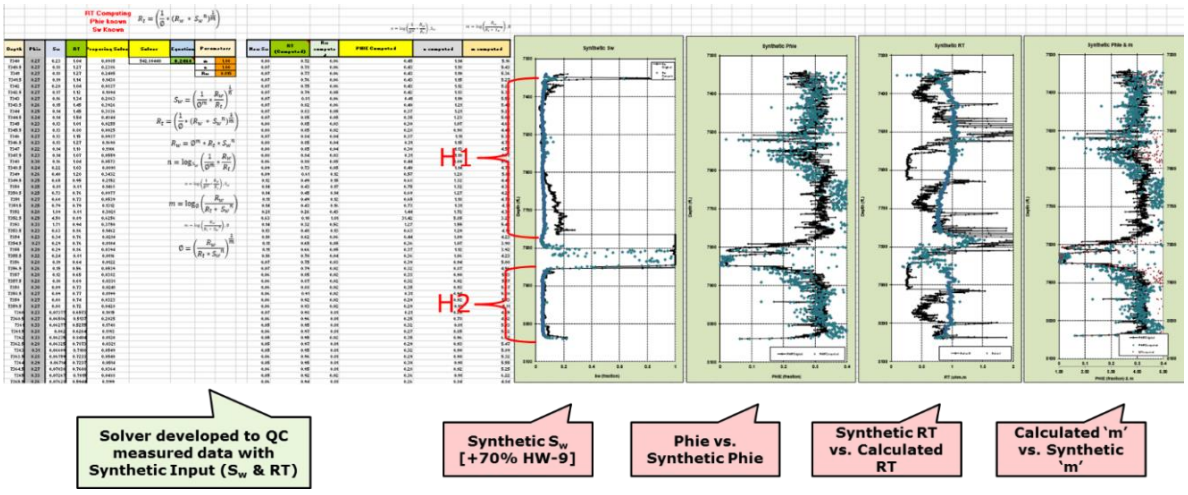

Figure 10: Synthetic water saturation profiles created for wells without resistivity data using a GRG Nonlinear Solver to back calculate the appropriate trends of petrophysical data for a given water saturation profile.

DOI: 10.17861/6e36e28d-50d9-4e31-9790-18db4bce6e5d

Supplementary Material

2.6 Saturation Height Modelling

Using drainage capillary pressure curves from our synthetic SCAL database, we generated water saturation height functions for all 43 wells under study and compared the results with the open hole derived water saturations. The Skelt-Harrison saturation function given by [3]

$$S_w = 1 - A * exp\left(-\left(\frac{B}{D + HAFWL}\right)^C\right), \quad (3)$$

where A, B, C and D are coefficients to match the capillary pressure curve for each RRT using a GRG Nonlinear Solver. Figures 11 and 12 show the comparison between open hole log S_w and SCAL S_w for different heights above FWL (e.g., crest – flank).

DOI: 10.17861/6e36e28d-50d9-4e31-9790-18db4bce6e5d

Supplementary Material

Figure 11 depicts the high-resolution distribution of water saturation for eight wells at different heights above the FWL (e.g., from crest to flank). In Figure 11 we also compare the water saturation derived from the open-hole logs and those from our saturation height functions. Our truth case has an undisclosed number of OWCs and capillary transition zone thicknesses.

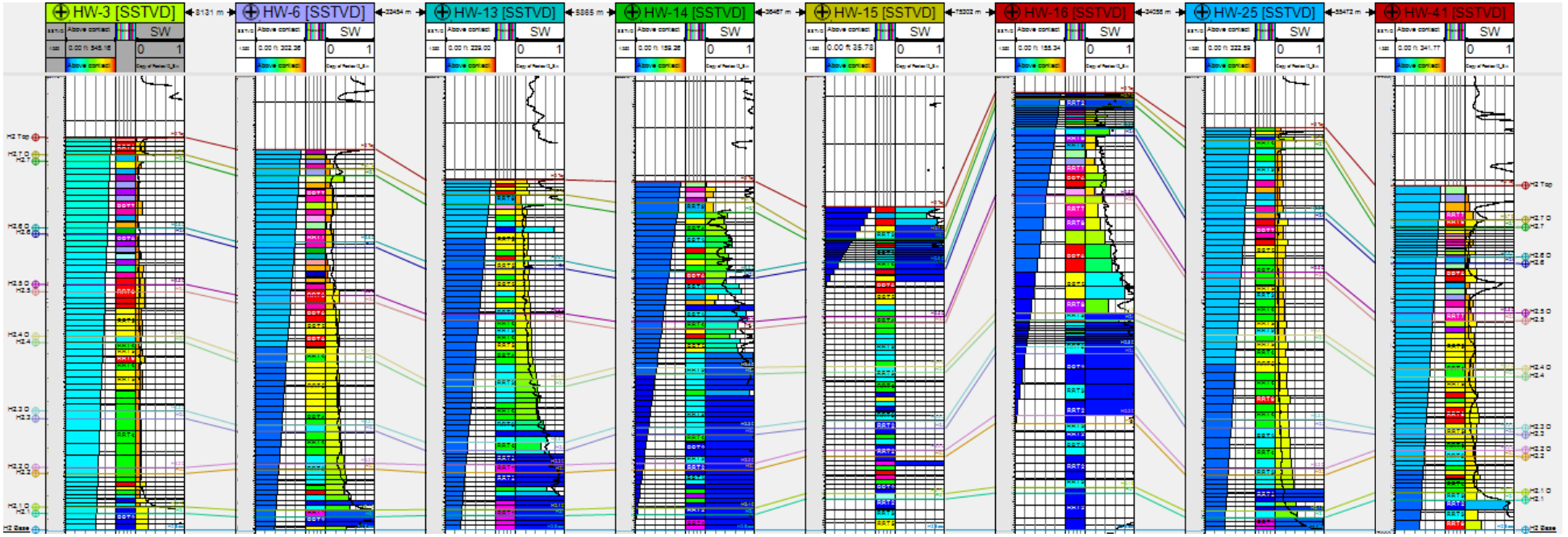

Figure 11: Eight example well logs and 3 tracks at multiple heights above the FWL. Height above the FWL (0 to 545 ft) [1st track], distribution of 27 reservoir rock types (1 to 27) [2nd track] and water saturation derived from our saturation height functions (upscaled) and the open-hole logs (continuous black line) [3rd track]. Water saturation ranges from 100% (blue) to 0% (dark orange). The reservoir rock typing methodology and the saturation height functions used have a good match with the water saturation derived from the open-hole logs. Scale fixed at 1:220 ft true vertical depth sub-sea. Depth is hidden in order to conceal the FWL of our truth case.

DOI: 10.17861/6e36e28d-50d9-4e31-9790-18db4bce6e5d

Supplementary Material

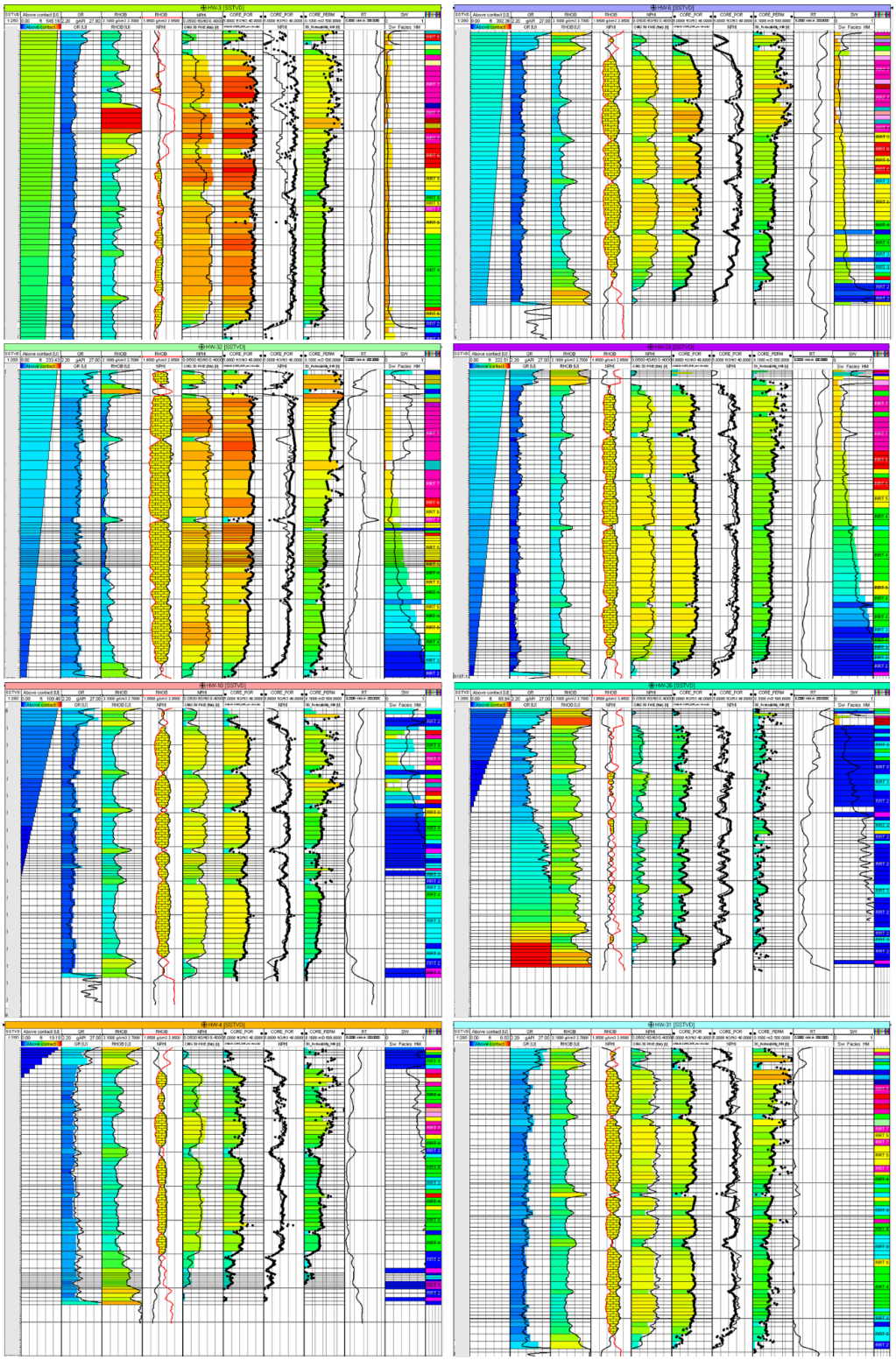

Figure 12: Eight example well logs and 11 tracks from multiple heights above the FWL. Height above the FWL (0 to 545 ft) [1st], gamma ray (2.2 to 27 gAPI) [2nd], density (2.1 to 2.7 g/cm^3) [3rd], density (1.9 to 2.9 g/cm^3) vs. neutron porosity (-0.15 to 0.45 ft^3/ft^3) [4th], neutron porosity (0.05 to 0.4 ft^3/ft^3) [5th], cored porosity (5 to 40 ft^3/ft^3) [6th], cored porosity vs. neutron porosity [7th], cored permeability (0.1 to 500 mD) [8th], formation resistivity (0.2 to 200 ohm) [9th], water saturation (0 to 100%) from saturation height functions (upscaled) and open-hole log water saturation (continuous black line) [10th] and reservoir rock types (1 to 27) [11th]. Scale fixed at 1:280 ft true vertical depth sub-sea (depth hidden).

DOI: 10.17861/6e36e28d-50d9-4e31-9790-18db4bce6e5d

Supplementary Material

2.7 Reservoir Characteristics

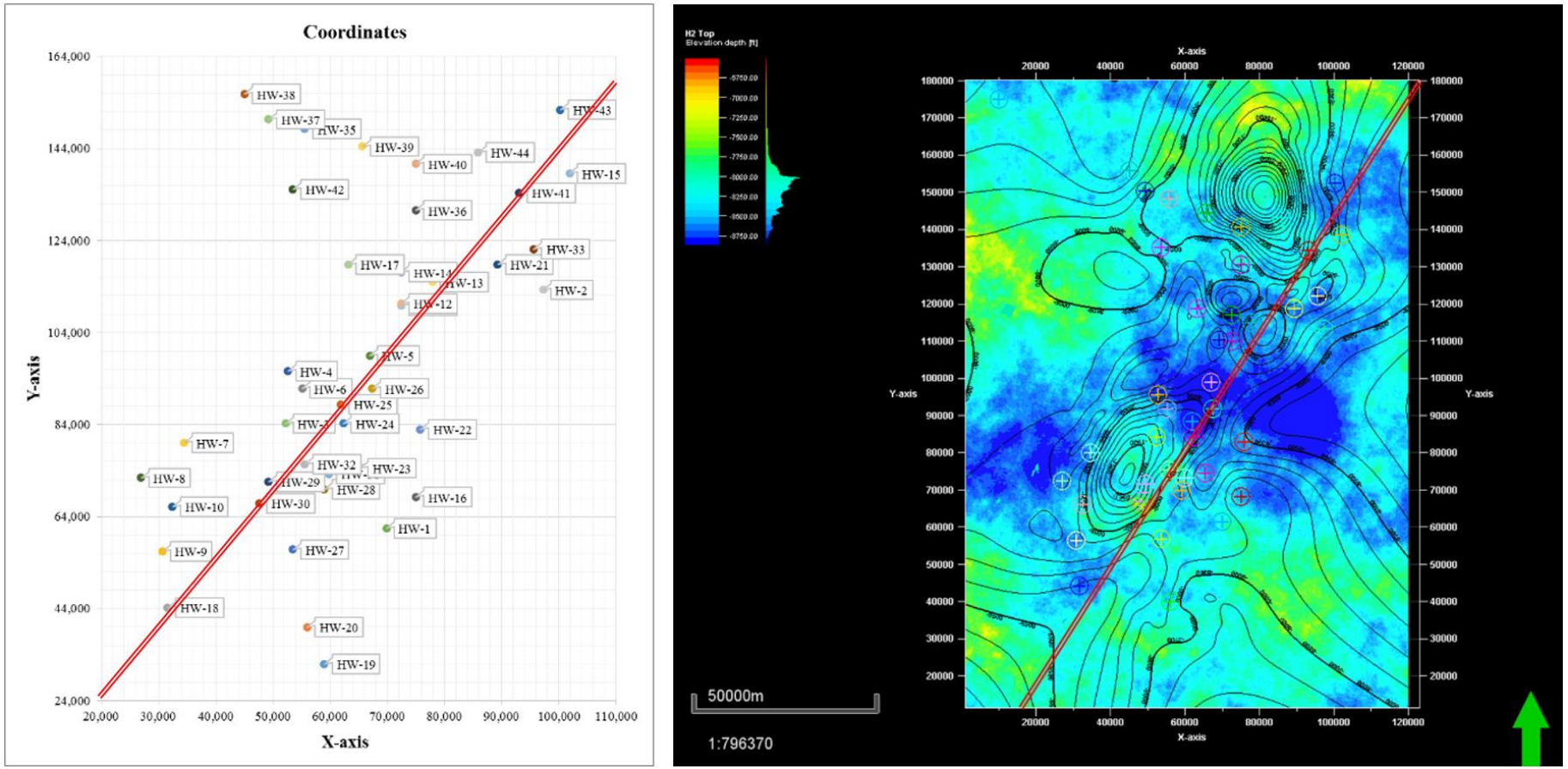

Figure 13: Wells and coordinates [left] and top depth map with synthetic contour lines [right]. The red line shows the 180 km cross section depicted in Figure 14 and Figure 15.

DOI: 10.17861/6e36e28d-50d9-4e31-9790-18db4bce6e5d

Supplementary Material

Shelf **Basin**

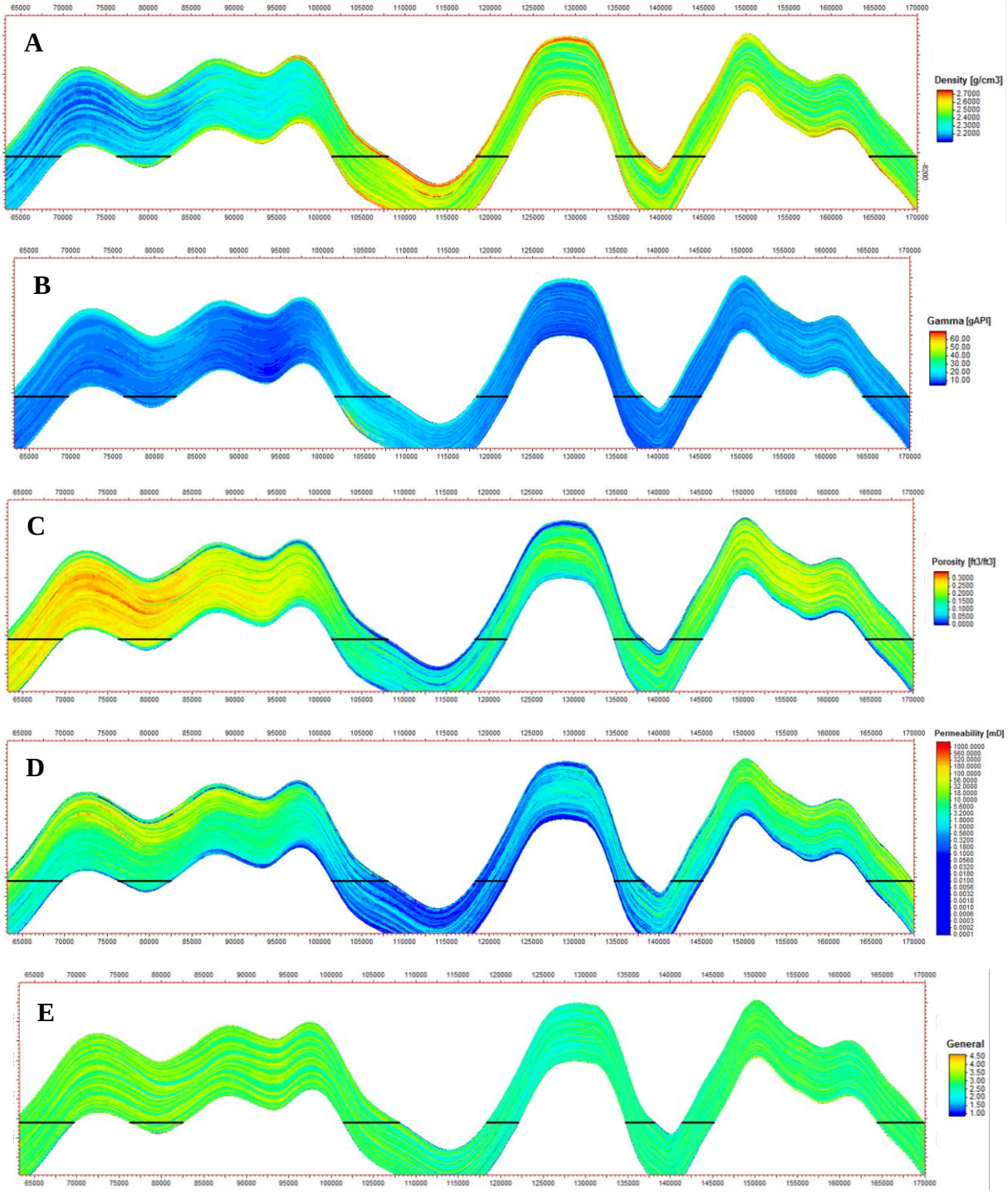

Figure 14: Cross sections (southwest to northeast ~180 km) showcasing multiple vertical and lateral petrophysical properties across the three structural closures found in our truth case. Density (2.1 to 2.7 g/cm^3) [A], gamma ray (2.2 to 70 gAPI) [B], porosity (0.05 to 0.35 ft^3/ft^3) [C], permeability (0.1 to 1500 mD) [D] and cementation exponent *m* (1 to 4.5) [E]. Our undisclosed free water level is exemplified as the black horizontal line (formation depth is hidden).

DOI: 10.17861/6e36e28d-50d9-4e31-9790-18db4bce6e5d

Supplementary Material

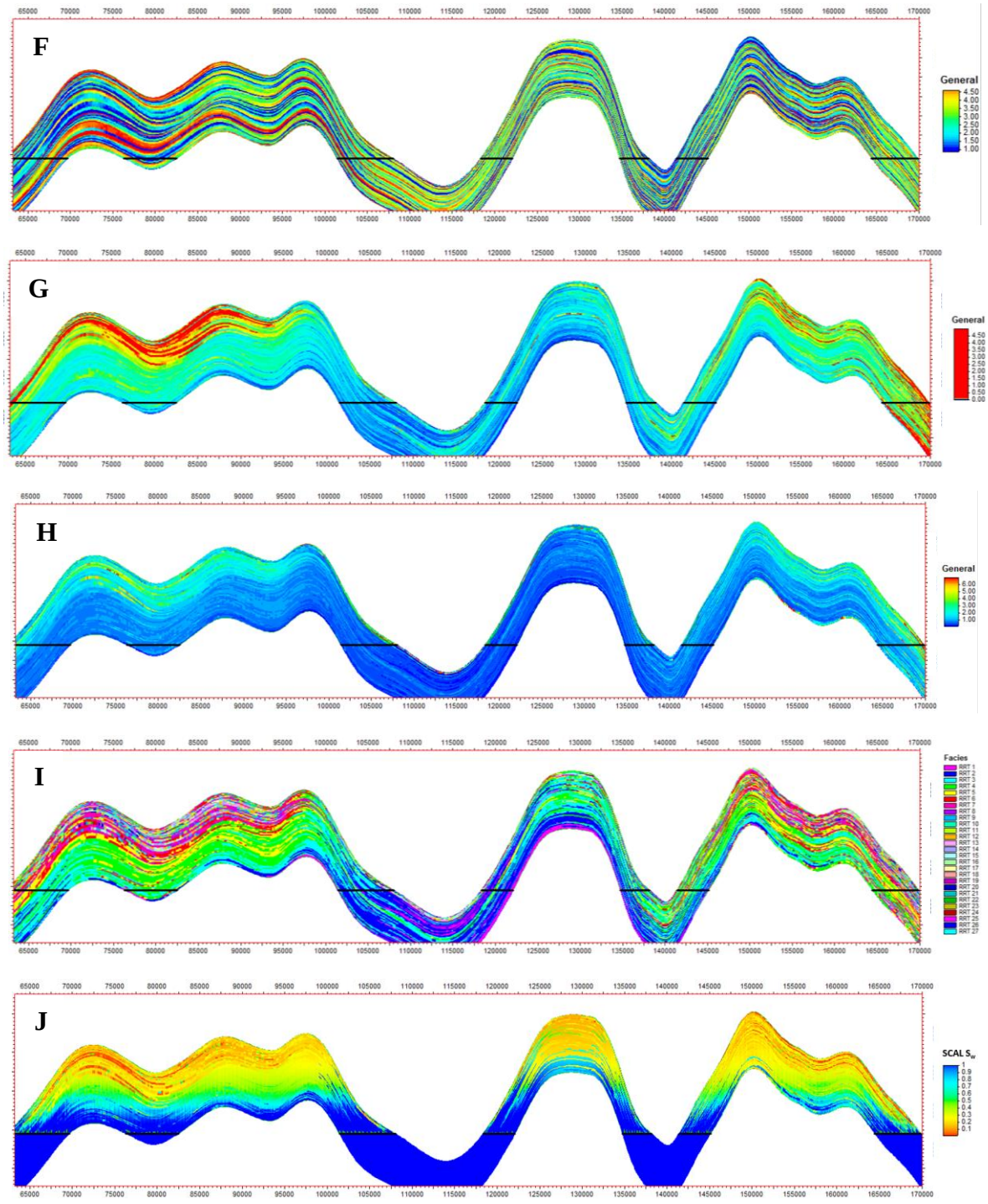

Figure 15: Cross sections (southwest to northeast ~180 km) showcasing multiple vertical and lateral petrophysical properties across the three structural closures found in our truth case. Saturation exponent *n* (1 to 4.5) [F], reservoir quality index (0 to 4.5) [G], Winland R35 mean pore throat size (0.1 to 7 µm) [H], reservoir rock types (1 to 27) [I] and water saturation (0 to 100%) [J]. Our undisclosed free water level is exemplified as the black horizontal line (formation depth is hidden).

DOI: 10.17861/6e36e28d-50d9-4e31-9790-18db4bce6e5d

Supplementary Material

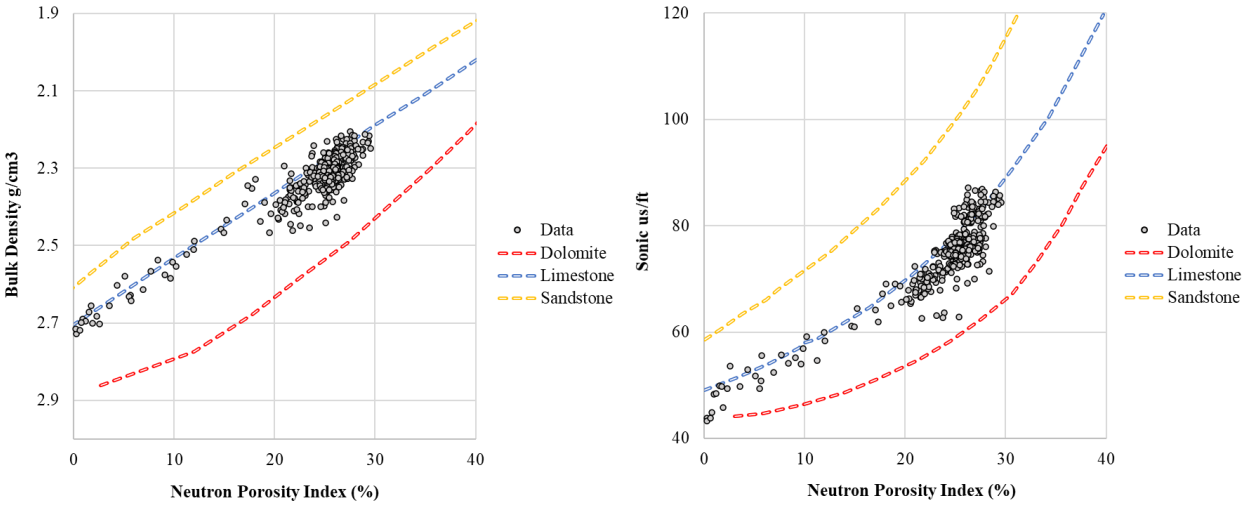

Figure 16: Lithology example of one particular well.

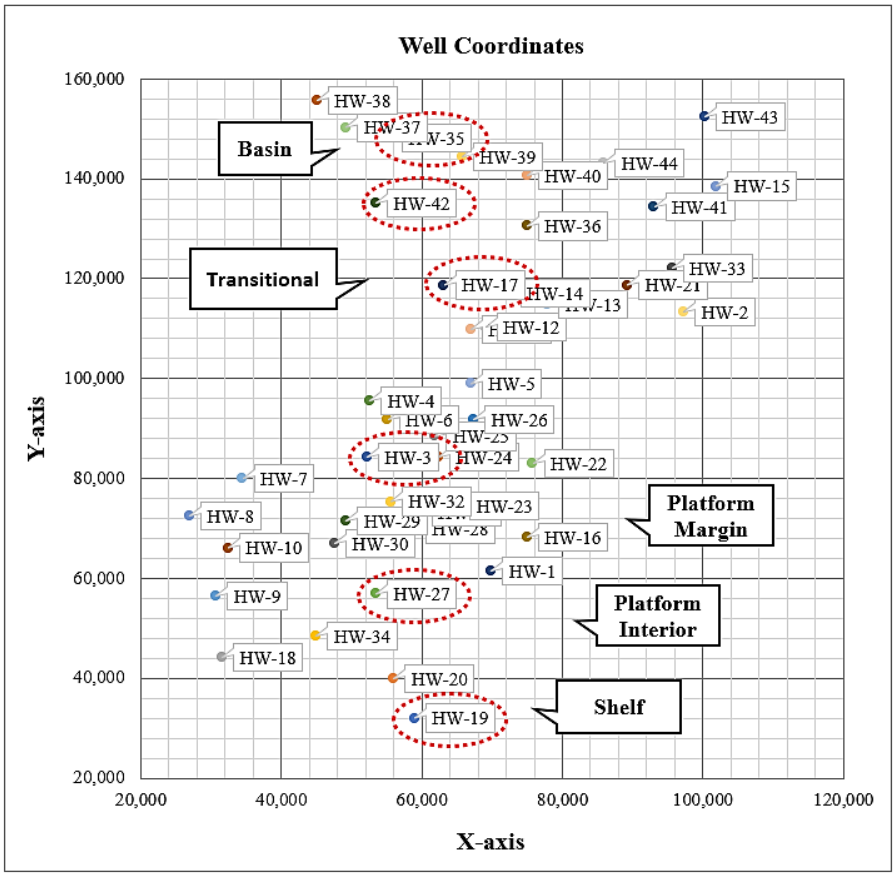

Figure 17: Well coordinates for all 43 wells used in this study along with the general location of the regional depositional environments. Highlighted in red are the six selected wells depicted in Figure 18 which highlight the regional heterogeneity variation across our model. The flow unit architectures across all wells are diverse but generally there is a trend; a more uniform flow and storage capacity in the shelf and basin areas and a more heterogeneous contrast in and around the platform interior – margin areas.

DOI: 10.17861/6e36e28d-50d9-4e31-9790-18db4bce6e5d

Supplementary Material

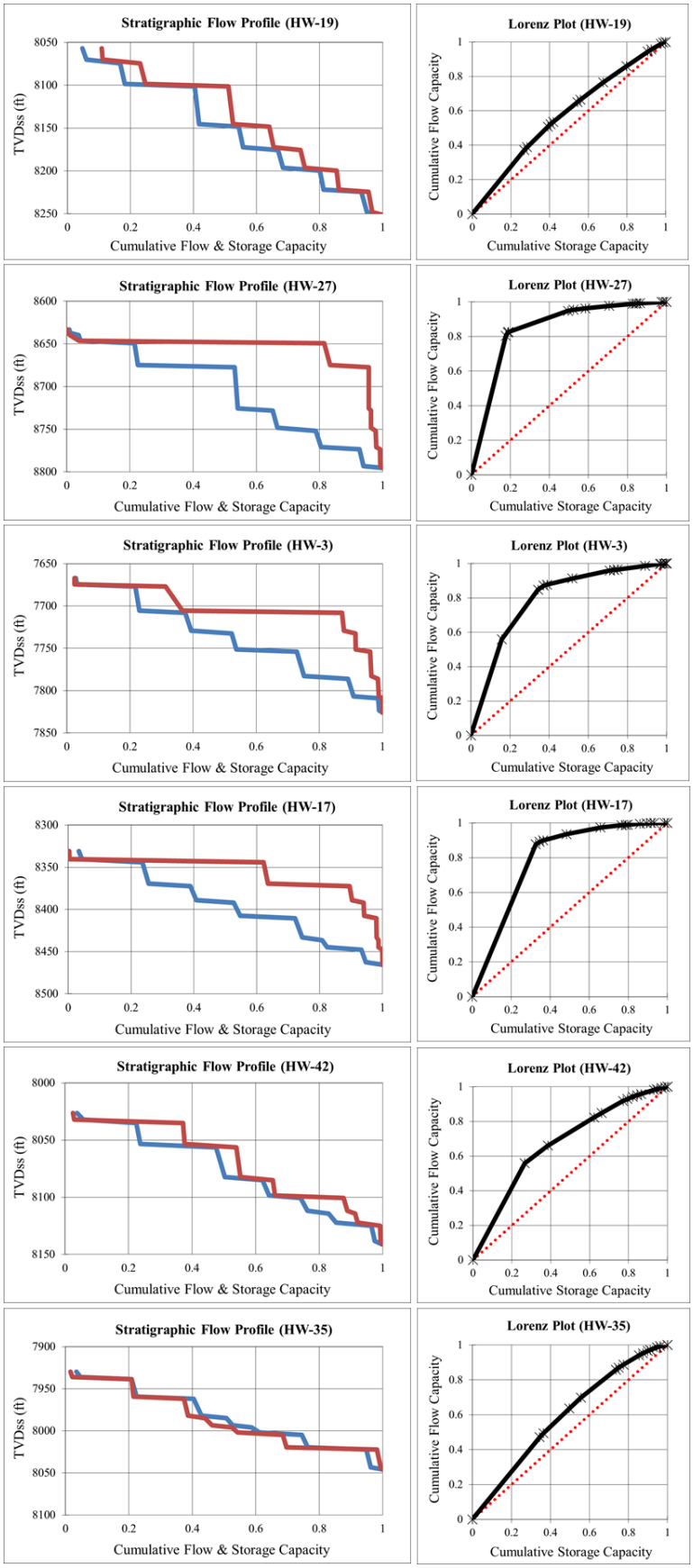

Figure 18: Regional flow unit architectures across the shelf-to-basin profile (Figure 17). Stratigraphic flow profiles have a normalized cumulative flow capacity (blue) and storage capacity (red) with respect to true vertical depth sub-sea.

DOI: 10.17861/6e36e28d-50d9-4e31-9790-18db4bce6e5d

Supplementary Material

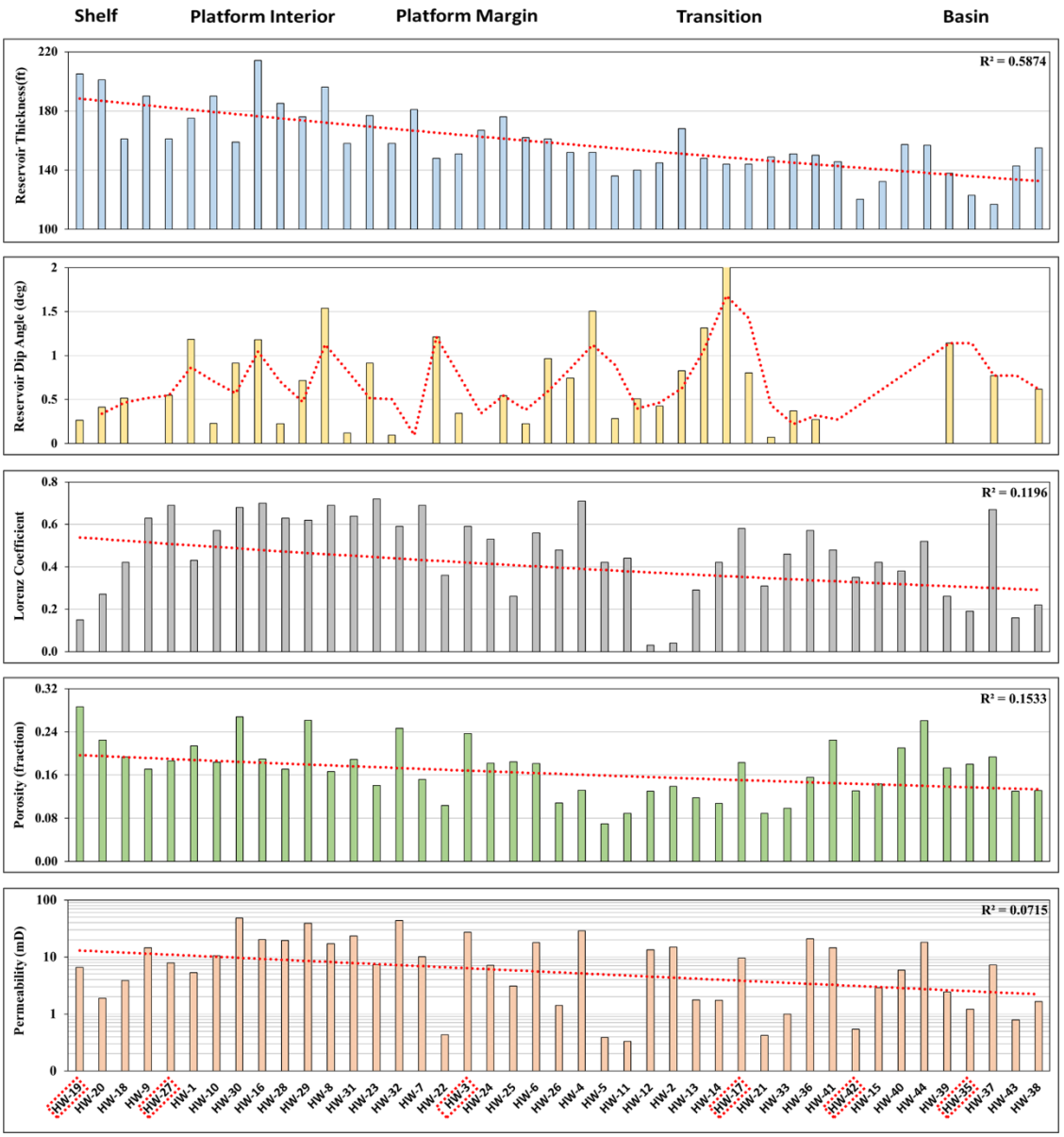

Figure 19: Key reservoir characteristics of all 43 wells used in this study ordered from lowest y-northing to highest y-northing (from shelf to basin). The six wells shown in Figure 17 and Figure 18 are also highlighted in red (x-axis).

DOI: 10.17861/6e36e28d-50d9-4e31-9790-18db4bce6e5d

Supplementary Material

2.8 Dynamic Reservoir Properties

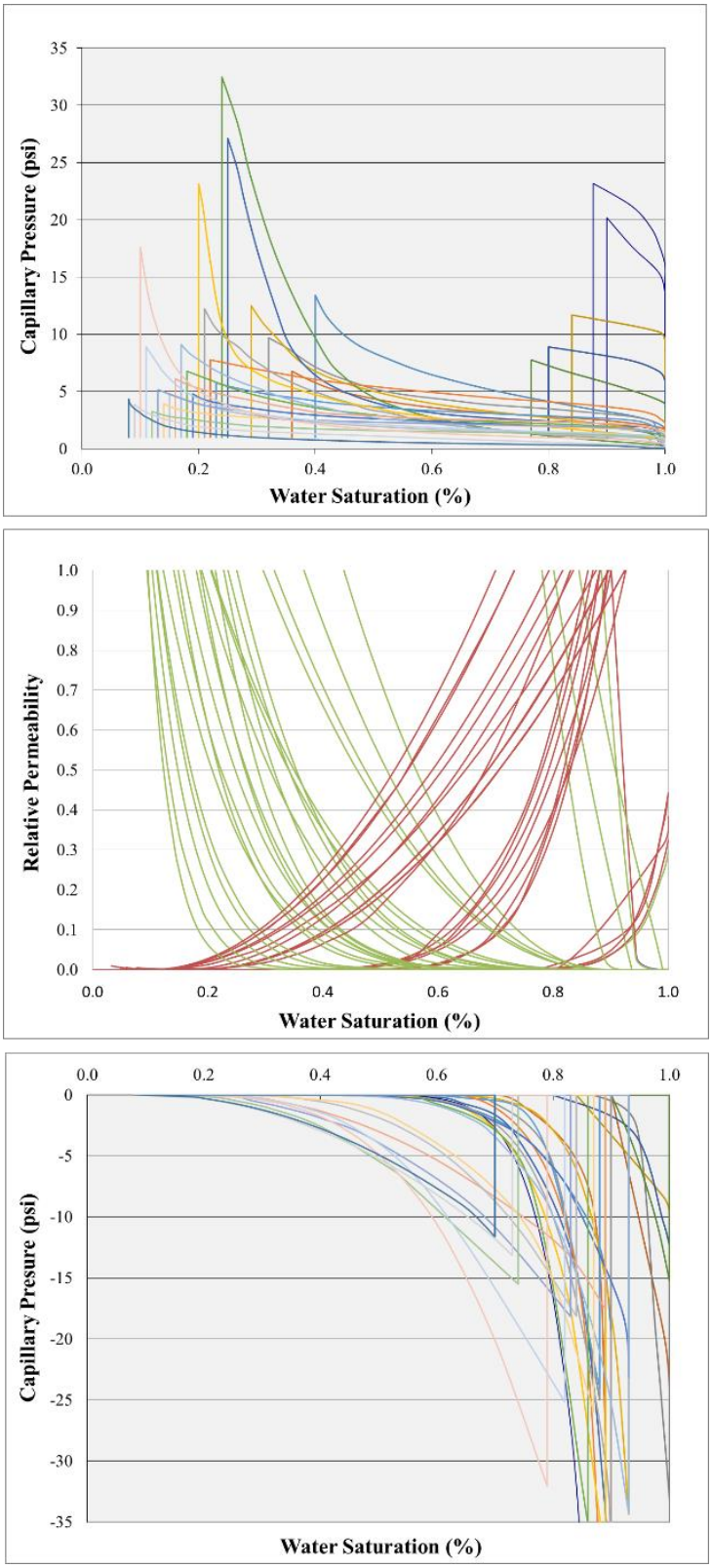

Figure 20: Drainage capillary pressure curves honouring irreducible water saturation cut-offs [top], the relative permeability of oil (green) and water (red) [centre], and forced imbibition capillary pressure curves honouring irreducible water saturation and residual oil saturation after waterflood cut-offs [bottom].

DOI: 10.17861/6e36e28d-50d9-4e31-9790-18db4bce6e5d

Supplementary Material

To generate forced imbibition (non-wetting phase displaced by wetting phase) capillary pressure curves we used a modified Skjaeveland equation (Eq. 4) [4]. To generate oil-water relative permeability curves we used the modified Brooks and Corey equations (Eq. 5 & 6) [5];

$$P_{cowi} = P_{cowstar} * \left(\frac{1 - S_w - S_{orw}}{1 - S_{wirr} - S_{orw}}\right)^{n_{cow+}} + P_{ceow} * \left(\frac{S_w - S_{orw}}{1 - S_{wirr} - S_{orw}}\right)^{n_{cow-}} \quad (4)$$

$$k_{rw} = k_{rwiro} * \left(\frac{S_w - S_{wirr}}{1 - S_{orw} - S_{wirr}}\right)^{n_w} \quad (5)$$

$$k_{row} = k_{rocw} * \left(\frac{1 - S_{orw} - S_w}{1 - S_{orw} - S_{wirr}}\right)^{n_o}, \quad (6)$$

where $P_{cowstar}$ is the capillary pressure maximum at S_{wirr}, S_{wirr} is the irreducible water saturation, S_{orw} is the residual oil saturation after waterflood, P_{ceow} is the capillary entry pressure, n_{cow+} and n_{cow-} are coefficients for the positive and negative sections of the forced imbibition capillary pressure curve. k_{rwiro} is the water relative permeability maximum at S_{wirr}, k_{rocw} is the oil relative permeability maximum at S_{wirr}, n_o and n_w are exponents for oil and water respectively.

Table 4: Correlations between relative permeability and wettability index.

Wettability	k_{rw} vs. k_{row} interception
Water Wet	> 0.7
Slightly Water Wet	0.55 - 0.7
Neutral	0.45 - 0.55
Slightly Oil Wet	0.45 - 0.3
Oil Wet	< 0.3

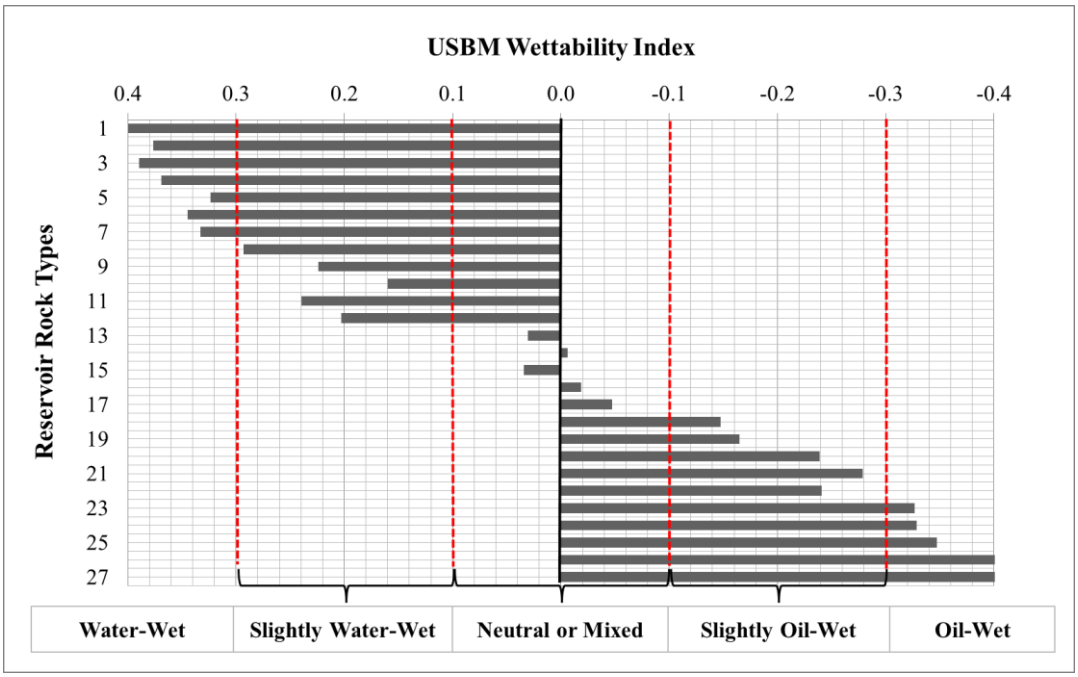

Figure 21: United States Bureau of Mines wettability index per reservoir rock type honouring the wettability, irreducible water saturation, and residual oil saturation after waterflood in the relative permeability curves.

DOI: 10.17861/6e36e28d-50d9-4e31-9790-18db4bce6e5d

Supplementary Material

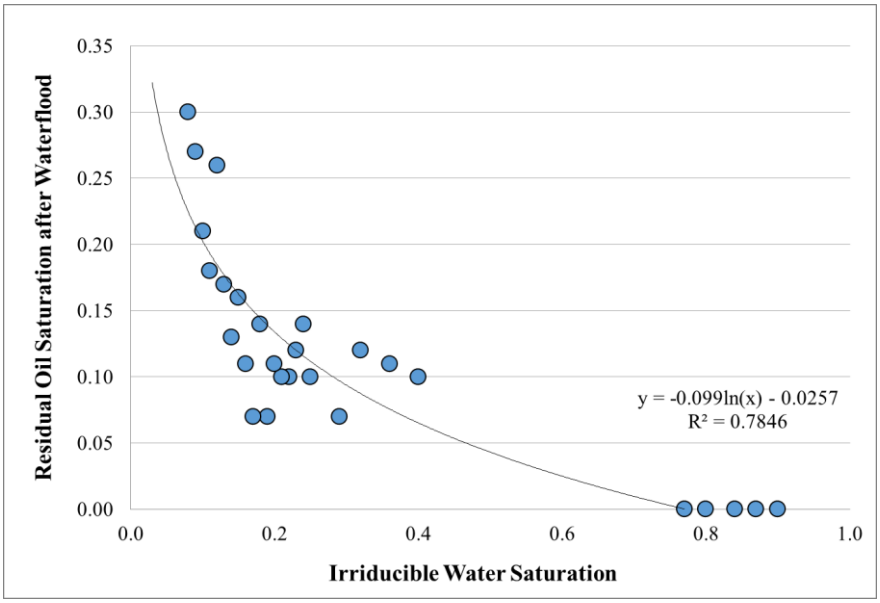

Figure 22: Synthetic relationship used between irreducible water saturation and residual oil saturation after waterflood for each reservoir rock type.

Figure 22 shows the synthetic results for irreducible water saturation and residual oil saturation after waterflood for each RRT used to calculate the wettability indexes. The wettability characteristics attempt to honour the following phenomena;

- High irreducible water saturation indicates water-wet tendency
- Intermediate irreducible water saturation indicates mixed-wet tendency
- Low irreducible water saturation indicates oil-wet tendency

DOI: 10.17861/6e36e28d-50d9-4e31-9790-18db4bce6e5d

Supplementary Material

Table 5: Dynamic characteristics of our 27 reservoir rock types for reservoir simulation. Conditional colours were applied to the wettability index column. USBM wettability index values range from strongly water wet (dark blue) to strongly oil wet (dark red).

RRTs	Winland R35 Cut-off (µm)	S_{wirr} (%)	S_{orw} (%)	Total Mobile Fluids (%)	k_{rw} & k_{ro} Interception	A_1 (Drainage P_c)	A_2 (Imbibition P_c)	USBM Wettability Index
1	0 - 0.2	0.9	0	0.1	0.94	1.73	0.67	0.41
2	0.2 - 0.4	0.87	0	0.13	0.94	2.57	1.08	0.38
3	0.4 - 0.6	0.84	0	0.16	0.95	1.74	0.71	0.39
4	0.6 - 0.8	0.8	0	0.2	0.92	1.59	0.68	0.37
5	0.8 - 1.0	0.77	0	0.23	0.88	1.37	0.65	0.32
6	1.0 - 1.2	0.4	0.1	0.5	0.73	3.45	1.56	0.34
7	1.2 - 1.4	0.36	0.11	0.53	0.72	2.26	1.05	0.33
8	1.4 - 1.6	0.32	0.12	0.56	0.7	3.12	1.59	0.29
9	1.6 - 1.8	0.29	0.07	0.64	0.67	3.1	1.85	0.22
10	1.8 - 2.0	0.25	0.1	0.65	0.59	3.99	2.76	0.16
11	2.0 - 2.2	0.24	0.14	0.62	0.57	4.65	2.68	0.24
12	2.2 - 2.4	0.23	0.12	0.65	0.55	2.68	1.68	0.2
13	2.4 - 2.6	0.22	0.1	0.68	0.52	3.95	3.68	0.03
14	2.6 - 2.8	0.21	0.1	0.69	0.5	2.68	2.72	-0.01
15	2.8 - 3.0	0.2	0.11	0.69	0.49	3.18	2.94	0.03
16	3.0 - 3.2	0.19	0.07	0.74	0.47	2.05	2.14	-0.02
17	3.2 - 3.4	0.18	0.14	0.68	0.53	2.53	2.82	-0.05
18	3.4 - 3.6	0.17	0.07	0.76	0.43	2.47	3.47	-0.15
19	3.6 - 3.8	0.16	0.11	0.73	0.42	2.56	3.74	-0.16
20	3.8 - 4.0	0.15	0.16	0.69	0.36	1.72	2.98	-0.24
21	4.0 - 4.6*	0.14	0.13	0.73	0.36	1.99	3.78	-0.28
22	4.6 - 5.0*	0.13	0.17	0.7	0.41	2.17	3.78	-0.24
23	5.0 - 5.5*	0.12	0.26	0.62	0.31	1.46	3.1	-0.33
24	5.5 - 6.0*	0.11	0.18	0.71	0.29	2.21	4.71	-0.33
25	6.0 - 6.2	0.1	0.21	0.69	0.28	2.28	5.07	-0.35
26	6.2 - 7.0*	0.09	0.27	0.64	0.24	1.05	2.74	-0.42
27	>7.0	0.08	0.3	0.62	0.23	0.74	2.23	-0.48

Table 5 showcases the dynamic characteristics of the RRTs used for reservoir simulation.

1 With degrading Winland R35 PTSDs, the samples' irreducible water saturation values are increasing. The relationship between irreducible water saturation and residual oil saturation after waterflood are showcased in Figure 20.
2 Total mobile fluids per RRT is the difference between irreducible water saturation and residual oil saturation after waterflood.
3 Areas for both A_1 and A_2 along with their respective USBM wettability indexes were computed.

DOI: 10.17861/6e36e28d-50d9-4e31-9790-18db4bce6e5d

Supplementary Material

3. Reservoir Model Description

Table 6: Dynamic reservoir model description for one ensemble member.

Reservoir Description	
Avg. Reservoir Length, km	60
Avg. Reservoir Width, km	26
Avg. North & South Flank Dip, degrees	0.6
Avg. East & West Flank Dip, degrees	1
Avg. Reservoir Thickness, ft	160
Shallowest Model Depth, ft	7,337
Deepest Model Depth, ft	8,461
Avg. FWL, ft	8,135
Reservoir Zones	8
Baffle Zones	7
Geological Layers	62
Avg. STOIIP, bbl.	$1.1x10^{9}$
Avg. Water Saturation, %	41
Reservoir Gridding	
Gridding	181*190*62
Grid Size (x & y), m	250
Grid Thickness Range, ft	0.8 – 8.0
Rock & Fluid Properties	
Avg. Porosity, %	21
Avg. Porosity Coefficient of Variation (Cv)	0.4
Avg. Permeability, mD	15
Avg. Permeability Coefficient of Variation (Cv)	1.8
Avg. Lorenz Coefficient	0.6
Rock Compressibility, 1/psi	$1*10^{-6}$
Reservoir Temperature, F	251
Water Compressibility, 1/psi	$3.7*10^{-6}$
Water Formation Volume Factor (FVF), RB/STB	1.06
Water Density, lb/ft3	65.34
Water Viscosity, cp	0.31
Water Salinity, ppm	157,482
Oil Density, lb/ft3	50.86
Oil Compressibility, 1/psi	$3*10^{-5}$
Oil Formation Volume Factor, RB/STB	1.53
Gas Oil Ratio (GOR), scf/STB	731
Gas Specific Gravity	0.6
Initial Conditions	
Initial Reservoir Pressure, psi	4,400
Reference Depth, ft	7,350
Bubble Point Pressure, psi	2,166
Relative Permeability Analytical Data	
Avg. Irreducible Water Saturation (S_{wirr}), fraction	0.32
Avg. Residual Oil Saturation after Waterflood (S_{orw}), fraction	0.12
Avg. Total Mobile Fluids, %	0.57
Avg. Relative Permeability to Water (k_{rw}) and Oil (k_{ro}) Interception, fraction	0.56

DOI: 10.17861/6e36e28d-50d9-4e31-9790-18db4bce6e5d

Supplementary Material

Table 7: Well controls for the initial full field development plan. A conservative BHP regulated production constraint was set to all the producers to be 334 psi above the bubble point. All water injectors were constrained only by BHP of 6,000 psi to be under the synthetic fracking pressure of this reservoir.

Vertical Producer Wells	
BHP Regulated Production, psi	2500
Rate Controlled Production, bbl./day	5,000
Perforations, layers	1-62
Vertical Infill Water Injectors	
BHP Regulated Injection Pressure, psi	6000
Perforations, layers	32-62
Vertical Peripheral Water Injectors	
BHP Regulated Injection Pressure, psi	6000
Perforations, layers	1-62

DOI: 10.17861/6e36e28d-50d9-4e31-9790-18db4bce6e5d

Supplementary Material

3.1 Subsectors

As part of the open-source COSTA Model dataset we also include seven small subsectors (C1 – C7) which originate from one ensemble member. These subsectors cover multiple structural locations capturing numerous reservoir architectures. All subsectors have an average dimension of 100 km^2 and 92,000 active grid blocks. The dynamic performance varies considerably e.g., water break through time, oil production (Figure 23).

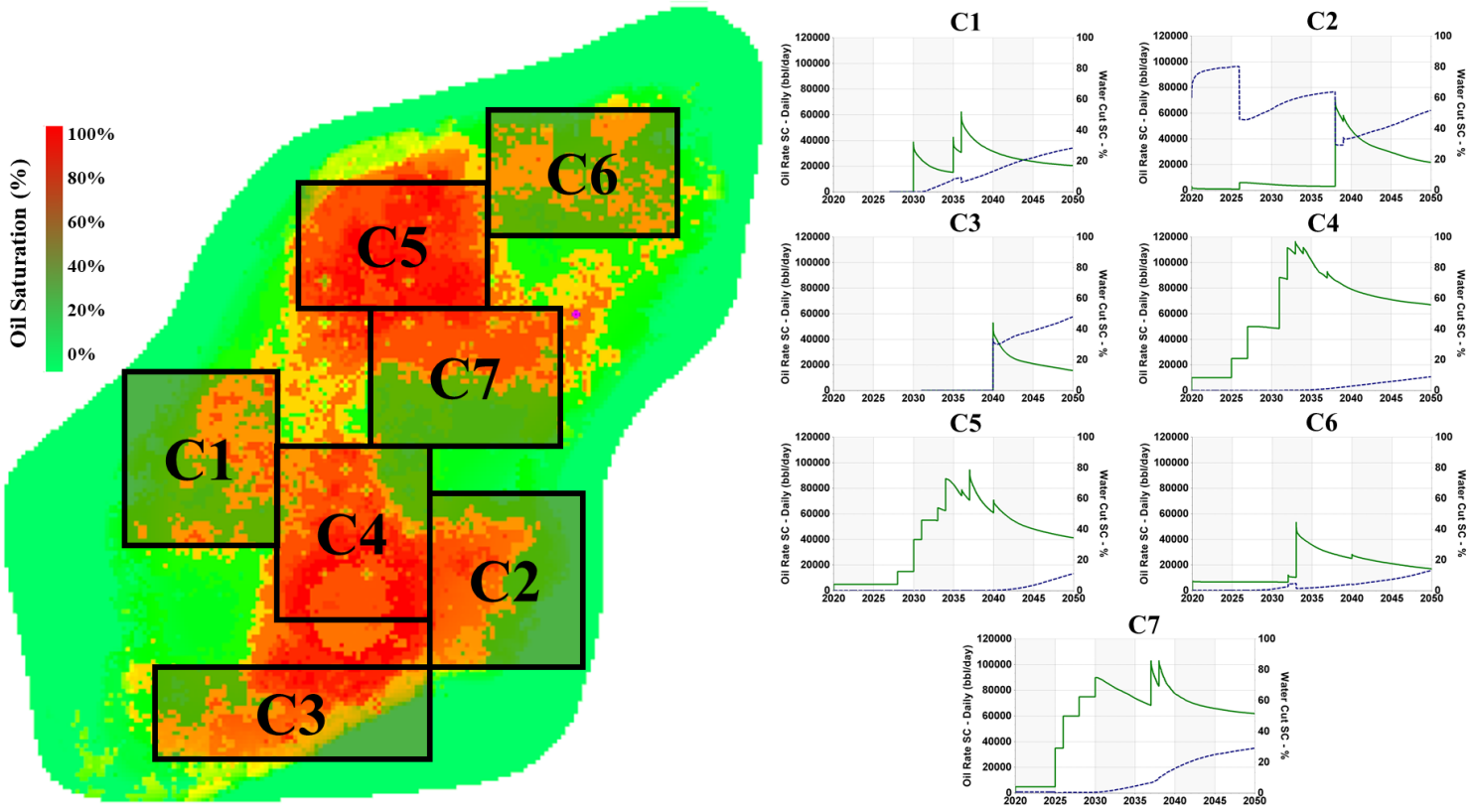

Figure 23: Location of our seven subsectors (C1 – C7) [left] and their field performances [right]. The subsectors incorporate the same field development plan with all 144 ensemble members and therefore some subsectors e.g., C3 start producing at a much later date (2040).

DOI: 10.17861/6e36e28d-50d9-4e31-9790-18db4bce6e5d

3.2 Skin Effect

All production wells that are a part of our truth case synthetic production data have been assigned variable, positive or negative, skin for each of the individual 248 producing wells. We assigned an undisclosed variable skin on all producer wells because in real fields the skin is often unknown and needs to be matched. All ensemble members which are a part of the open-source package have been assigned a skin effect of zero.

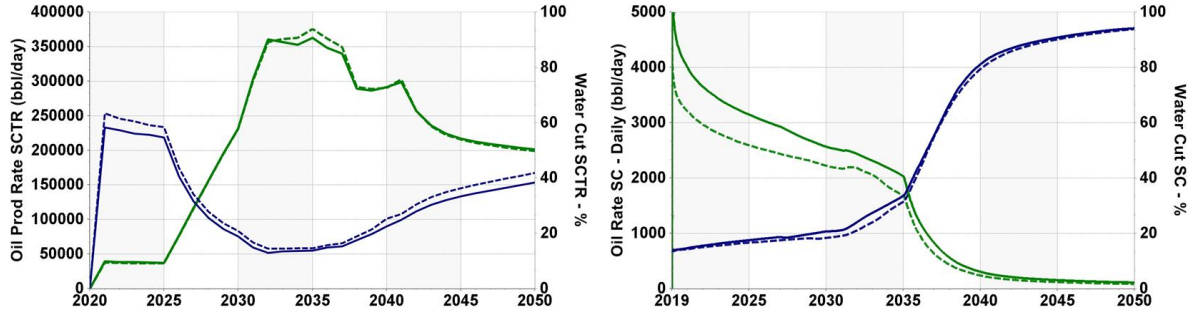

Figure 24: Field performance comparison of a case with zero skin (solid lines) and case with positive and negative skin randomly selected for each of the individual 248 producing wells (dashed lines) [left]. An example of a single producer well with a negative skin (solid line) helping improve the oil production rate [right].

DOI: 10.17861/6e36e28d-50d9-4e31-9790-18db4bce6e5d

Supplementary Material

3.3 RRT Effect

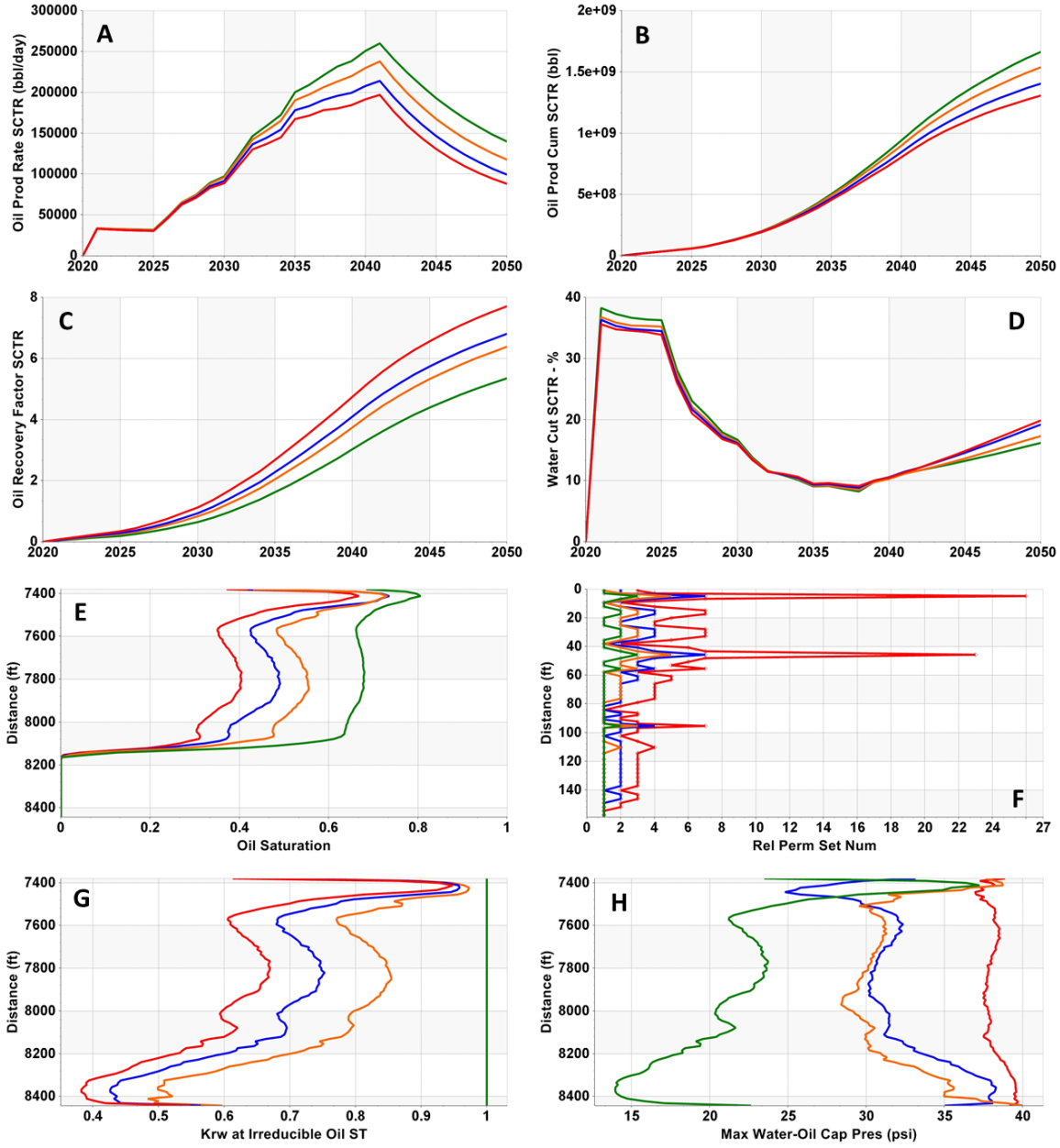

Figure 25: Field performance and reservoir characterisation of a single ensemble member with four clustered reservoir rock type maps; 27 RRTs [red], 7 RRTs [blue], 5 RRTs [orange] and 3 RRTs [green]. Oil production rate [A], oil production cumulative [B], oil recovery factor [C], water-cut [D], average field oil saturation with height above the FWL [E], rock type distribution along a single well [F], average field relative permeability to water at irreducible oil [G] and average field maximum oil-water capillary pressure [H].

DOI: 10.17861/6e36e28d-50d9-4e31-9790-18db4bce6e5d

Supplementary Material

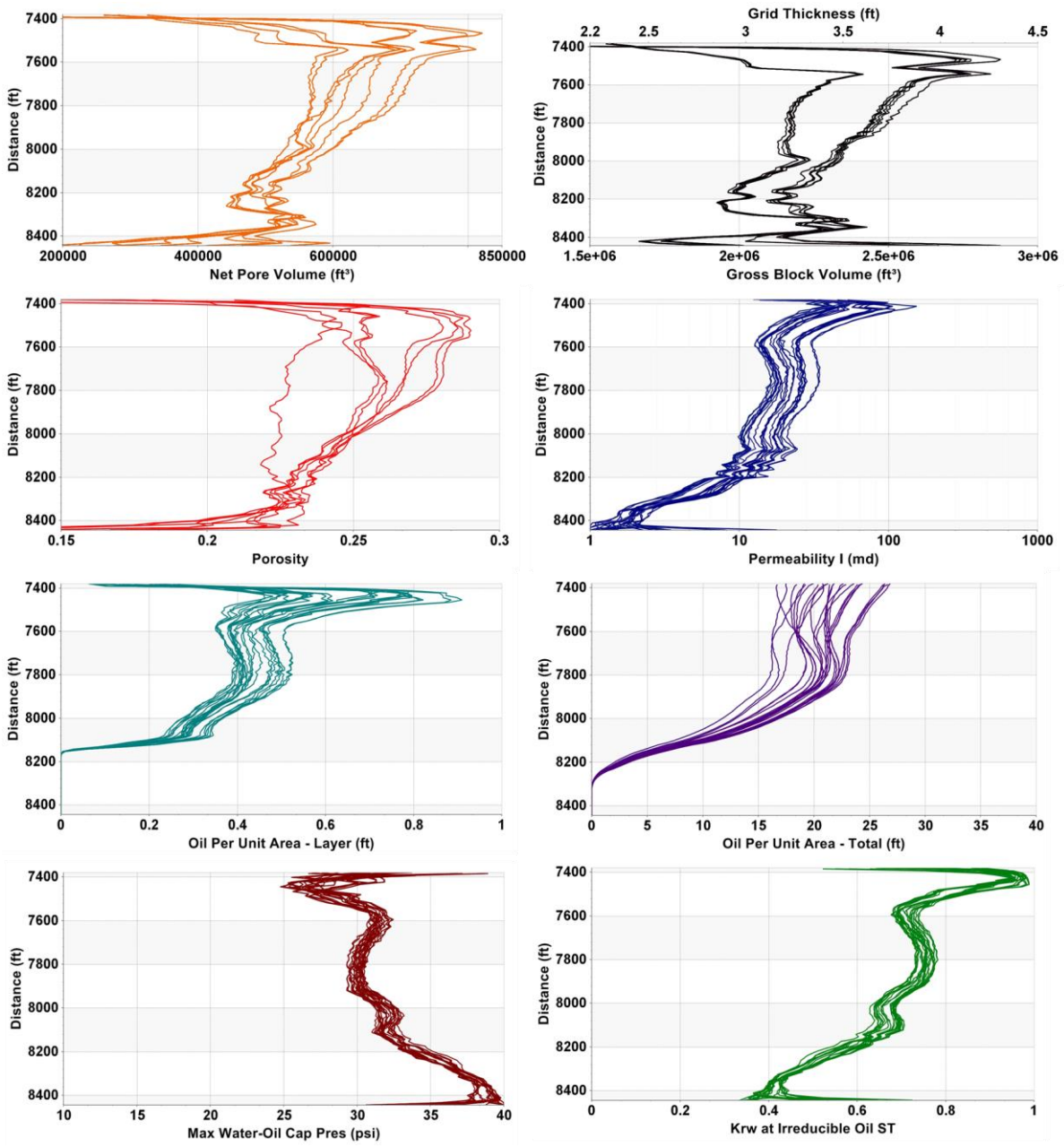

Figure 26: Laterally averaged properties for a given reservoir layer across all ensemble members with 7 RRTs. Differences in net pore volume, gross block volume and grid thickness are associated with having two different stratigraphic frameworks concepts e.g., the interpretation of the formation tops, baffle tops and their respective thicknesses. Wide range of average field values for porosity are due to the use of wireline or cored values. Permeability profiles vary due to the well-log upscaling technique used and spatial modelling approach (linked to facies maps). Both porosity and permeability have also been modelled with a reduced horizontal anisotropic range. Differences in oil per unit area (layer), oil per unit area (total), average field maximum oil-water capillary pressure, and average field relative permeability to water at irreducible oil are also demonstrated.

DOI: 10.17861/6e36e28d-50d9-4e31-9790-18db4bce6e5d

Supplementary Material

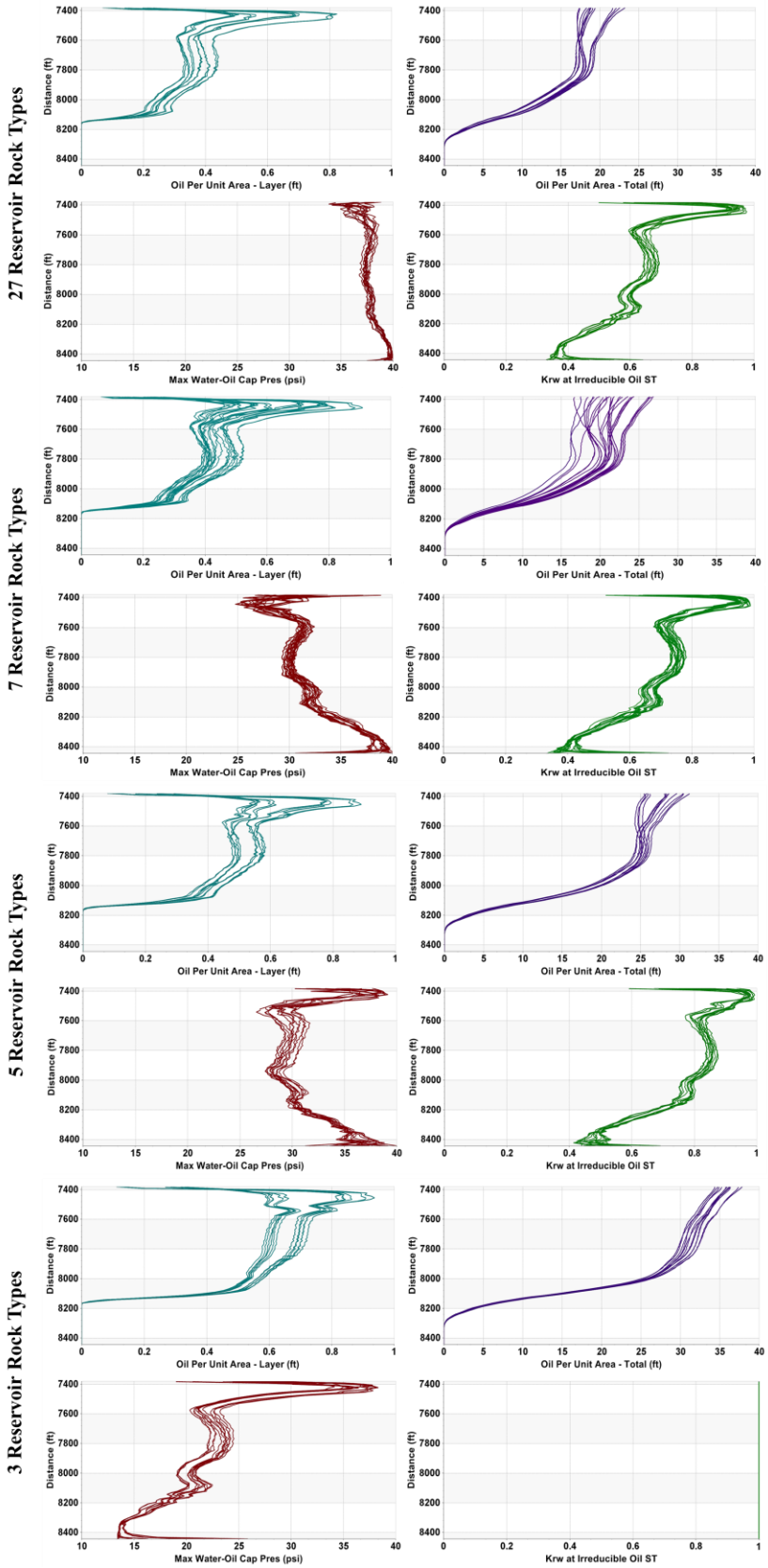

Figure 27: Laterally averaged properties for a given reservoir layer for all ensemble members with a variable number of reservoir rock types e.g., 3, 5, 7 and 27 RRTs showing the differences in oil per unit area (layer), oil per unit area (total), maximum water-oil capillary pressure and relative permeability of water at irreducible oil with respect to reservoir height.

DOI: 10.17861/6e36e28d-50d9-4e31-9790-18db4bce6e5d

Supplementary Material

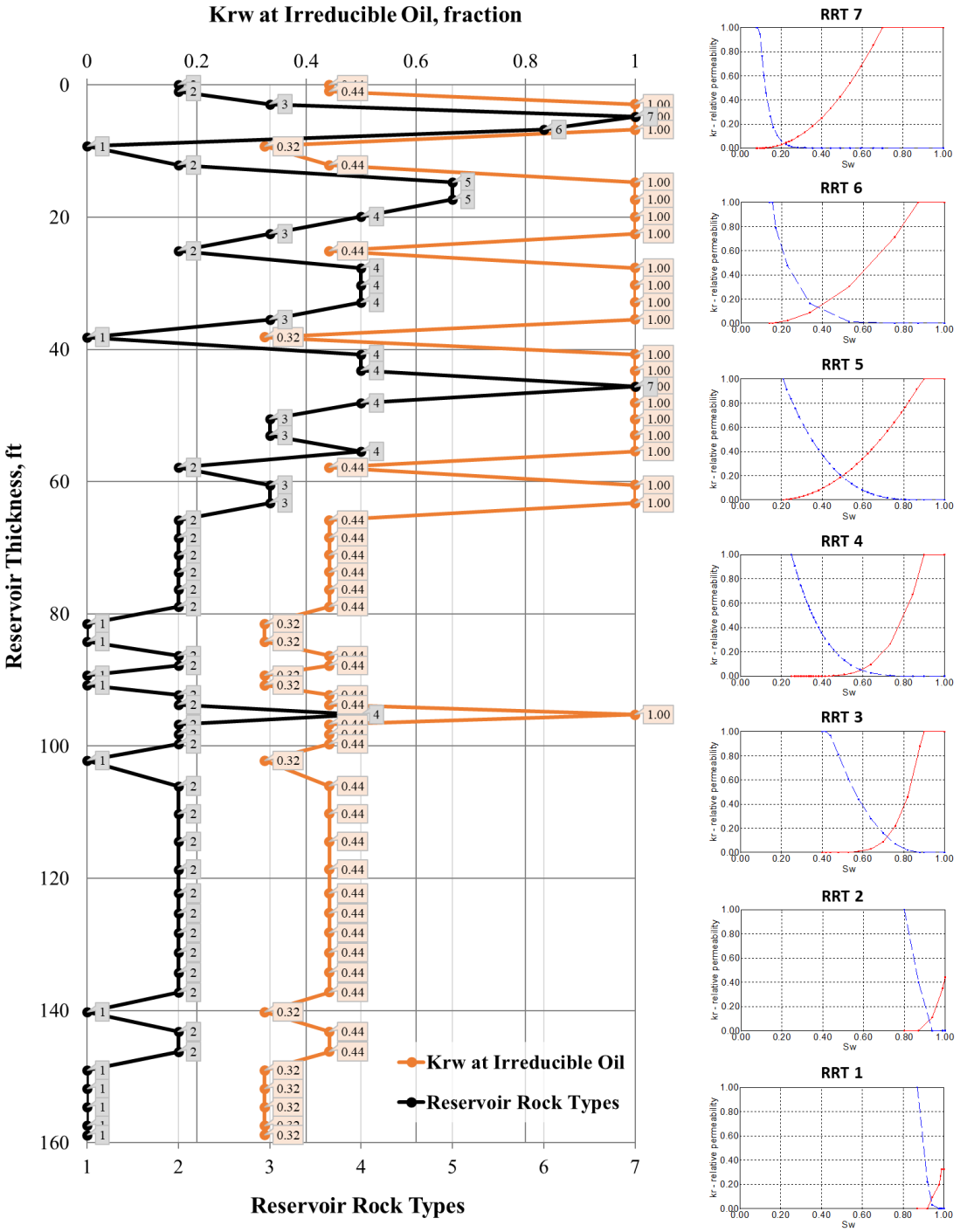

Figure 28: Distribution of relative permeability of water at irreducible oil and reservoir rock types along well HW-10. The seven relative permeability curves used in this particular ensemble member are also shown. Wettability varies from strongly water-wet (RRT 1) to strongly oil-wet (RRT 7).

DOI: 10.17861/6e36e28d-50d9-4e31-9790-18db4bce6e5d

Supplementary Material

3.4 Grid Refinement & Ultimate Recovery Factor

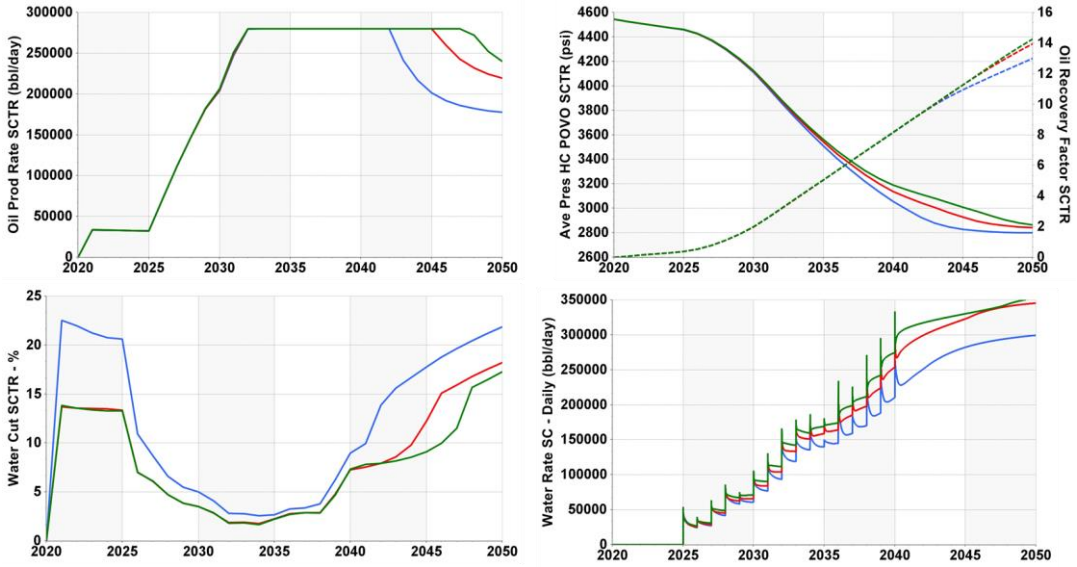

Figure 29: Field performance affected by grid refinement for one ensemble member. Original model grid dimension 250 x 250 m [blue], 125 x 125 m [red] and 62.5 x 62.5 m [green].

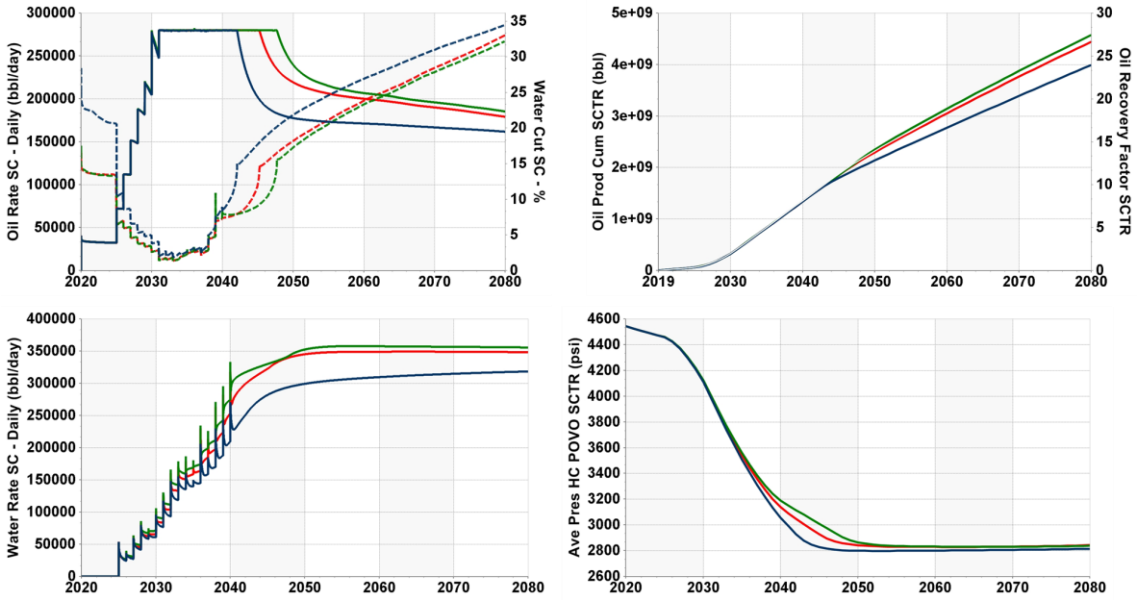

Figure 30: Ultimate recovery factor and field performance affected by grid refinement for one ensemble member. Original model grid dimension 250 x 250 m [blue], 125 x 125 m [red] and 62.5 x 62.5 m [green].

DOI: 10.17861/6e36e28d-50d9-4e31-9790-18db4bce6e5d

Supplementary Material

3.5 Synthetic Production Data

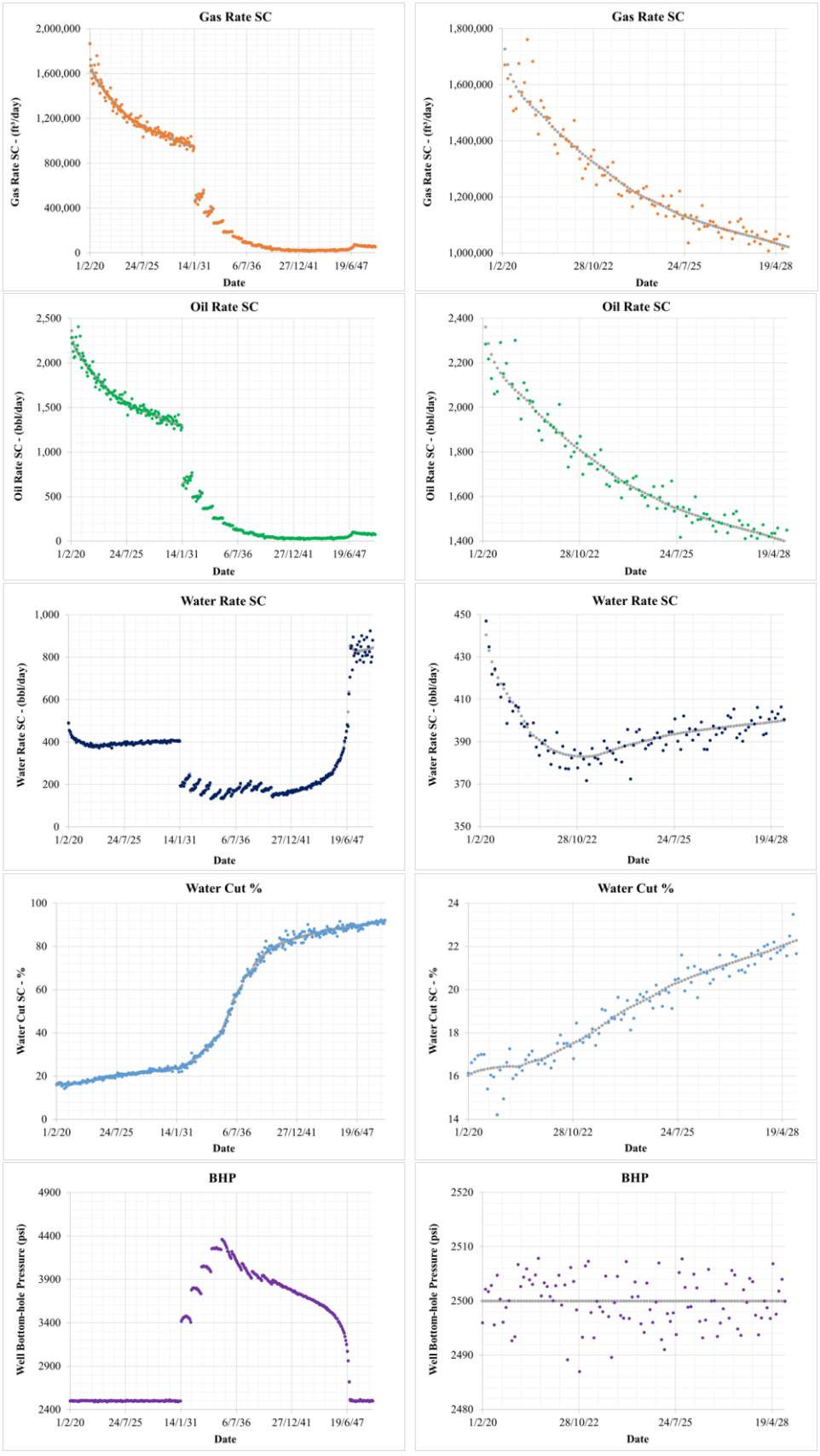

Figure 31: Random Gaussian noise added synthetic production data. Showcased side-by-side are zoomed in time sections for a particular well.

DOI: 10.17861/6e36e28d-50d9-4e31-9790-18db4bce6e5d

Supplementary Material

4. Understanding the Data

Supplementary data associated with this article can be found in the data repository for the COSTA model at https://doi.org/10.17861/6e36e28d-50d9-4e31-9790-18db4bce6e5d.

- **144 open-source reservoir simulation (CMG IMEX) & 3D Geo-Models (PETREL)**

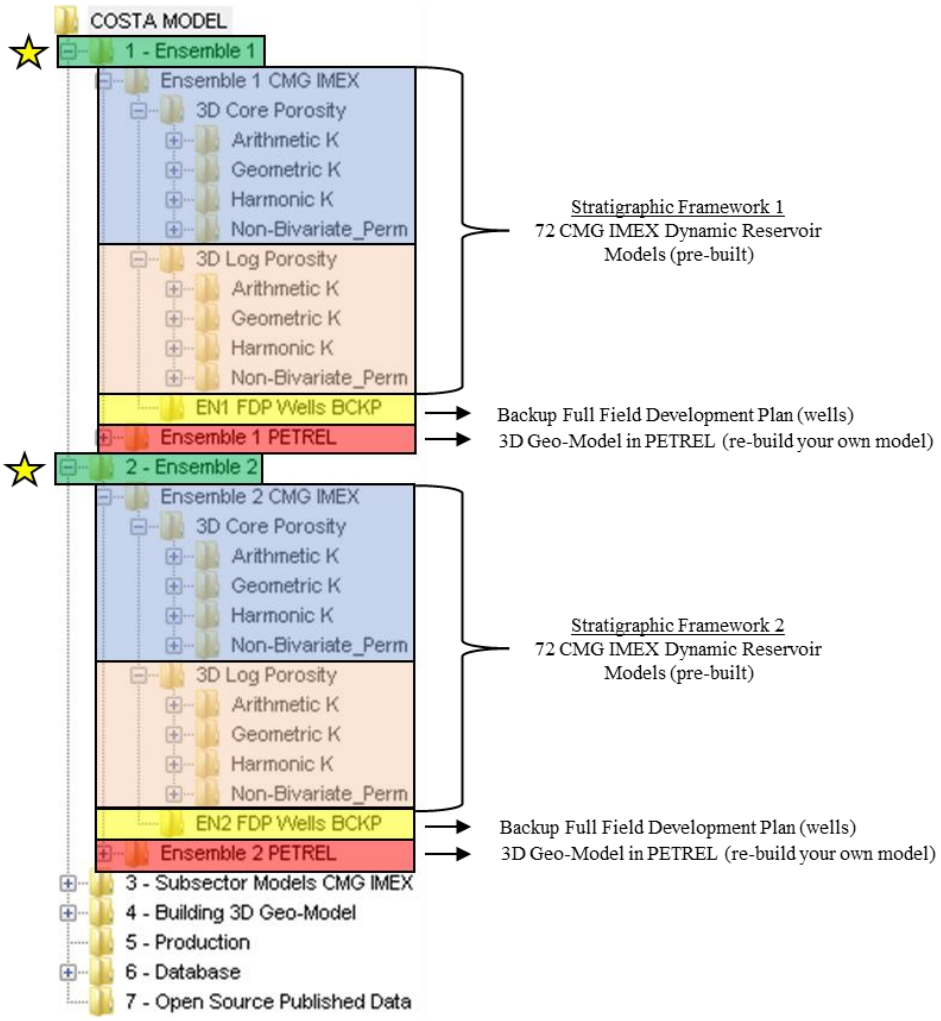

- **Seven cropped subsector reservoir simulation models (CMG IMEX)**

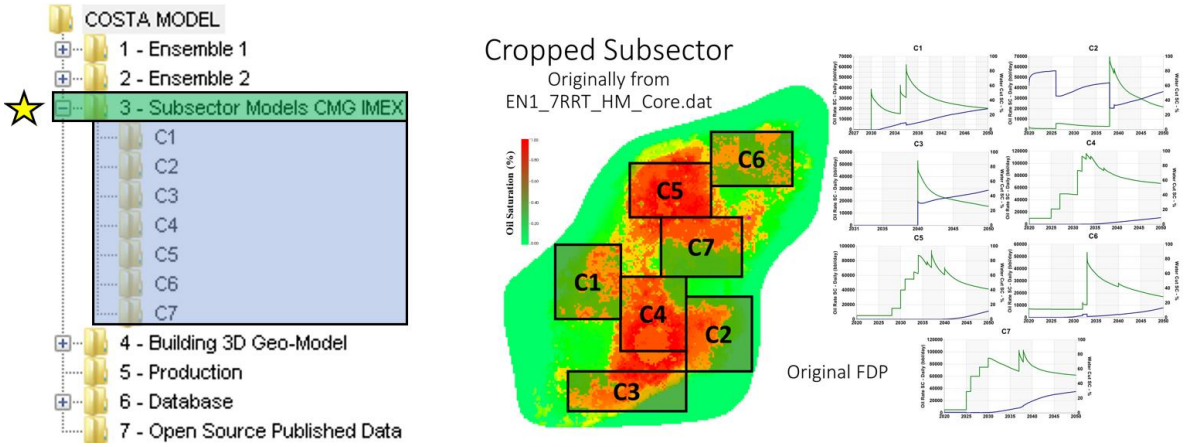

DOI: 10.17861/6e36e28d-50d9-4e31-9790-18db4bce6e5d

Supplementary Material

- **Data to build your own 3D Geo-Model (well heads, well logs & contour maps)**

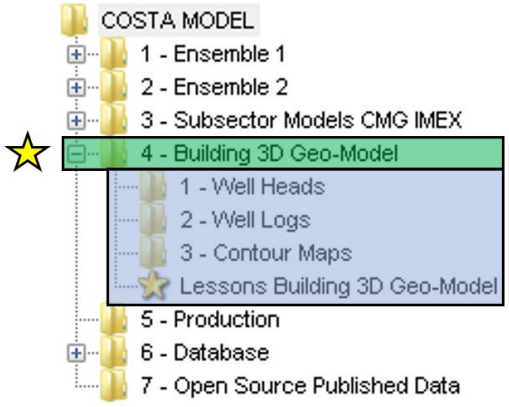

Well Heads

well No	Easting X	Northing Y	KB	TD
HW-1	69895	61474	466	9117
HW-2	97263	113263	1133	9943
HW-3	52211	84211	160	8299
HW-4	52632	95579	29	8625
HW-5	66947	98947	36	8640
HW-6	55158	91789	49	8396
HW-7	34526	80000	367	8984
HW-8	26947	72421	416	9103
HW-9	30737	56421	492	9074
HW-10	32421	66105	397	8920
HW-11	72421	109895	34	8677
HW-12	69053	1103316	74	8685
HW-13	77895	114947	30	8428
HW-14	72421	117053	42	8518
HW-15	101895	138526	74	8637
HW-16	74947	68211	397	8905
HW-17	63158	118737	69	8850
HW-18	31579	44211	474	9350
HW-19	58947	32000	336	8904
HW-20	56000	40000	322	8918
HW-21	89263	118737	150	8682
HW-22	75789	82947	356	9287
HW-23	65263	74526	424	9256
HW-24	62316	84211	426	8867
HW-25	61895	88421	386	8728
HW-26	67368	91789	375	8932
HW-27	53474	56842	453	9114
HW-28	58947	69895	430	9025
HW-29	49263	71579	466	8682
HW-30	47579	66947	590	8848
HW-31	59789	73263	417	9081
HW-32	55579	75368	441	8873
HW-33	95579	122105	138	8594
HW-35	55579	148211	77	8435
HW-36	74947	130526	79	8632
HW-37	49263	150316	74	8563
HW-38	45053	155789	89	8880
HW-39	65684	144421	499	8687
HW-40	74947	140632	1312	9297
HW-41	93053	134316	82	8371
HW-42	53474	135158	75	8529
HW-44	85895	143158	71	7533

Well Logs

```
# LAS format log file from PETREL
# Project units are specified as depth units
#~~~~~~~~~~~~~~~~~~~~~~~~~~~~~~~~~~~~~~~~~~~~~~~~~~~~~~~~~~~~~~~~~~~~~~~~~~~~~~~
~version Information
VERS.   2.0:
WRAP.   NO:
#~~~~~~~~~~~~~~~~~~~~~~~~~~~~~~~~~~~~~~~~~~~~~~~~~~~~~~~~~~~~~~~~~~~~~~~~~~~~~~~
~Well
STRT .ft        8150.0 :
STOP .ft        8630.0 :
STEP .ft        0.5    :
NULL .          -999.25  :
COMP.           : COMPANY
WELL.  HW-10    : WELL
FLD.   COSTA    : FIELD
LOC.            : LOCATION
SRVC.           : SERVICE COMPANY
DATE.  2018-02-05 14:15:39   : Log Export Date (yyyy-MM-dd HH:mm:ss)
PROV.           : PROVINCE
UWI.   HW-10    : UNIQUE WELL ID
API.            : API NUMBER
#~~~~~~~~~~~~~~~~~~~~~~~~~~~~~~~~~~~~~~~~~~~~~~~~~~~~~~~~~~~~~~~~~~~~~~~~~~~~~~~
~Curve
DEPT .ft                    : DEPTH
GR .GAPI                    : GR
RHOB .g/cm3                 : RHOB
NPHI .ft3/ft3               : NPHI
DT .us/ft                   : DT
PHIE .ft3/ft3               : PHIE
RT .ohm.m                   : RT
SW .                        : SW
SO .                        : SO
CORE_POR .ft3/ft3           : CORE_POR
CORE_PERM .mD               : CORE_PERM
~Parameter
#~~~~~~~~~~~~~~~~~~~~~~~~~~~~~~~~~~~~~~~~~~~~~~~~~~~~~~~~~~~~~~~~~~~~~~~~~~~~~~~
~Ascii
8440.0  31.66   2.73    0.07    -999.25 0.00    17.62   -999.25 -999.25 -999.25 -999.25
8440.5  30.61   2.73    0.06    -999.25 0.00    19.01   -999.25 -999.25 -999.25 -999.25
8441.0  29.37   2.72    0.06    -999.25 0.00    20.33   -999.25 -999.25 -999.25 -999.25
8441.5  28.05   2.73    0.05    -999.25 0.00    21.58   -999.25 -999.25 -999.25 -999.25
8442.0  27.10   2.73    0.05    -999.25 0.00    22.79   -999.25 -999.25 -999.25 -999.25
8442.5  26.20   2.75    0.06    -999.25 0.00    24.12   -999.25 -999.25 -999.25 -999.25
8443.0  25.70   2.75    0.06    -999.25 0.00    25.53   -999.25 -999.25 -999.25 -999.25
8443.5  26.20   2.74    0.06    -999.25 0.00    26.56   -999.25 -999.25 -999.25 -999.25
8444.0  26.74   2.74    0.05    -999.25 0.00    26.72   -999.25 -999.25 -999.25 -999.25
8444.5  26.31   2.74    0.05    -999.25 0.00    26.20   -999.25 -999.25 -999.25 -999.25
8445.0  26.06   2.75    0.04    -999.25 0.00    25.54   -999.25 -999.25 -999.25 -999.25
8445.5  27.39   2.75    0.04    -999.25 0.00    25.15   -999.25 -999.25 -999.25 -999.25
8446.0  29.68   2.74    0.05    -999.25 0.00    25.23   -999.25 -999.25 -999.25 -999.25
8446.5  30.68   2.73    0.05    -999.25 0.00    25.72   -999.25 -999.25 -999.25 -999.25
8447.0  29.68   2.73    0.05    -999.25 0.00    26.46   -999.25 -999.25 -999.25 -999.25
```

- **Synthetic production for history matching**

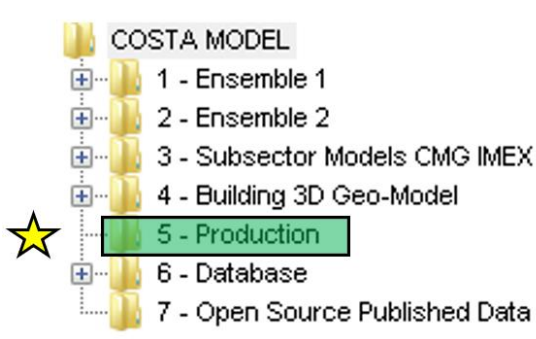

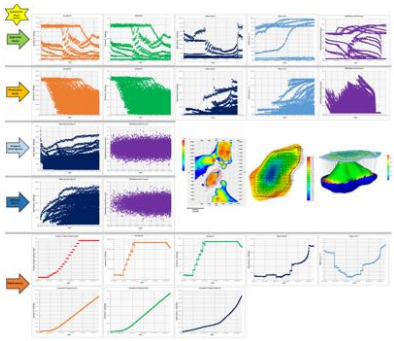

- **Database (SCAL, saturation height functions, relative permeability tables etc.)**

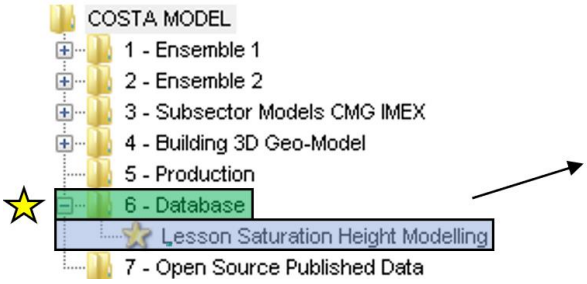

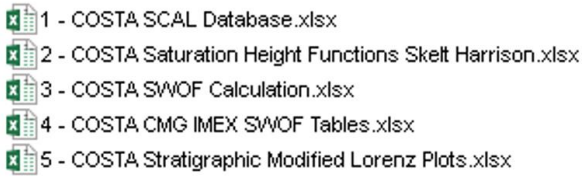

- **List of relevant literature for the COSTA MODEL**

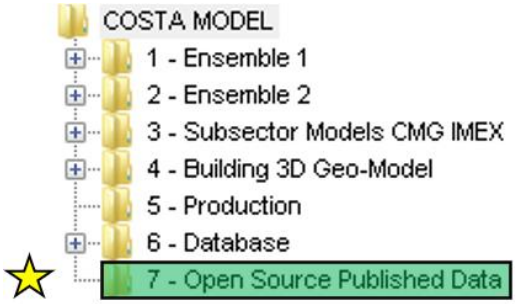

DOI: 10.17861/6e36e28d-50d9-4e31-9790-18db4bce6e5d

Supplementary Material

5. References

[1] G. E. Archie, "The electrical resistivity log as an aid in determining some reservoir characteristics," *Transactions of the AIME,* vol. 146, no. 01, pp. 54-62, 1942.

[2] H. Winland, D., "Evaluation of Gas Slippage and Pore Aperture Size in Carbonate and Sandstone Reservoirs.," 1976, No. F76-G-5.

[3] B. Harrison and X. Jing, "Saturation height methods and their impact on volumetric hydrocarbon in place estimates," 2001.

[4] S. M. Skjaeveland, L. M. Siqveland, A. Kjosavik, W. L. H. Thomas, and G. A. Virnovsky, "Capillary Pressure Correlation for Mixed-Wet Reservoirs," *SPE Reservoir Evaluation & Engineering*, vol. 3, no. 01, pp. 60-67, 2000/2/1/ 2000, doi: 10.2118/60900-PA.

[5] R. H. Brooks and A. T. Corey, "Hydraulic Properties of Porous Media," *Hydrology Papers*, vol. Colorado State University, 1964.

DOI: 10.17861/6e36e28d-50d9-4e31-9790-18db4bce6e5d